

Ericksen number and Deborah number cascade predictions of a model for liquid crystalline polymers for simple shear flow

D. Harley Klein and L. Gary Leal^{a)}

Department of Chemical Engineering, University of California at Santa Barbara,
Santa Barbara, California 93106

Carlos J. García-Cervera and Hector D. Ceniceros

Department of Mathematics, University of California at Santa Barbara,
Santa Barbara, California 93106

(Received 20 September 2006; accepted 22 November 2006; published online 7 February 2007)

We consider the behavior of the Doi-Marrucci-Greco (DMG) model for nematic liquid crystalline polymers in planar shear flow. We found the DMG model to exhibit dynamics in both qualitative and quantitative agreement with experimental observations reported by Larson and Mead [Liq. Cryst. **15**, 151 (1993)] for the Ericksen number and Deborah number cascades. For increasing shear rates within the Ericksen number cascade, the DMG model displays three distinct regimes: stable simple shear, stable roll cells, and irregular structure accompanied by disclination formation. In accordance with experimental observations, the model predicts both ± 1 and $\pm 1/2$ disclinations. Although ± 1 defects form via the *ridge-splitting* mechanism first identified by Feng, Tao, and Leal [J. Fluid Mech. **449**, 179 (2001)], a new mechanism is identified for the formation of $\pm 1/2$ defects. Within the Deborah number cascade, with increasing Deborah number, the DMG model exhibits a streamwise banded texture, in the absence of disclinations and roll cells, followed by a monodomain wherein the mean orientation lies within the shear plane throughout the domain. © 2007 American Institute of Physics. [DOI: 10.1063/1.2424499]

I. INTRODUCTION

The potential for application of liquid-crystalline polymers (LCPs)¹⁻³ as a structural material relies upon the fact that there is a high degree of alignment at both the molecular and mesoscopic levels. The relative *order* within the material is a strong function of its processing history. In fiber-spinning flows, the flow is largely extensional and this enhances the natural tendency of the LCP to exist in an aligned state. A result is the well-known Kevlar® fiber produced by DuPont. Unfortunately, the processing of LCPs in other configurations is limited by the fact that there is a propensity for the formation and proliferation of orientational defects, known as disclinations, especially in the shear-type flows that are characteristic of most other polymer processing applications. The result in these cases is a material that is isotropic at the mesoscopic level, with alignment confined to small microdomains, and the intrinsic advantage of LCPs as a structural material (which might otherwise offset its increased cost compared to other polymeric materials) is lost. Therefore, to realize the full potential of LCPs, we must understand the processes by which disclinations are formed, and the dependence of these processes on the flow conditions. Because of the small-scale nature of the instabilities that lead to defects in LCPs, the usefulness of macroscopic experimental studies of such instabilities is limited. Reliance is, therefore, placed on theory and numerical investigations for detailed insight into the topological evolution of liquid-crystalline systems. Mesoscale numerical investigations, in

which a continuum description couples the microscale structure to the macroscopic stress, allow for qualitative prediction of the effects of flow conditions on the formation of disclinations.

Nematic LCPs exhibit both elastic and viscoelastic characteristics when subjected to flow. Both elasticity and viscoelasticity in this class of materials emanate from the equilibrium tendency for alignment in a uniform direction. Elasticity is associated with the resistance to the formation of *spatial gradients* in the mean molecular orientation, and is generally known as *Frank* or *gradient elasticity*.⁴ Viscoelasticity derives from flow-induced deviations in the degree of alignment at each point from its equilibrium value. Corresponding to these two manifestations of elastic effects, there are two dimensionless measures of the shear rate for flows of liquid-crystalline polymers. The first, known as the Ericksen number² Er , is a ratio of the magnitude of viscous shear stress to the elastic stress. The second is known as the Deborah number⁵ De , and is the product of the shear rate and the natural relaxation time for reestablishment of an equilibrium orientation state. In real systems, the Ericksen number is generally several orders of magnitude larger than the Deborah number at any fixed shear rate. Although there have been many experimental investigations of the behavior of LCPs in planar shear flow,⁶⁻¹³ the most comprehensive, in terms of observations over a wide range of shear rates (and thus also a wide range of Ericksen and Deborah numbers) is the study of Larson and Mead^{10,11} in which a nematic liquid-crystalline poly(γ -benzyl-glutamate) (PBG) solution was subjected to shear flows in torsional and planar cells. Larson and Mead¹¹ observed that this LCP exhibited two distinct regimes when

^{a)}Electronic mail: lg120@engineering.ucsb.edu

subjected to shear flow, which are now believed to be generic to all LCPs. The two regimes are referred to as the Ericksen number and Deborah number cascades.

The Ericksen number cascade corresponds to the regime of shear rates where $Er \geq \mathcal{O}(1)$ and $De \ll 1$ and is characterized by instabilities that arise at low shear rates as a consequence of the competition between the viscous stress imposed by the flow and long-range (gradient) elasticity. The result at low to moderate Ericksen numbers is the formation of banded patterns (i.e., a birefringent striped texture) oriented either perpendicular to or along the flow direction, the direction of which depends upon the initial mean molecular orientation. As the shear rate is increased, this is followed by increasingly complex time-dependent flows, and ultimately, to the evolution of disclinations that proliferate with time and lead to a polydomain structure in which the system is only aligned in small microdomains but is isotropic on larger length scales. During the whole series of flow types described above, though the Ericksen number can achieve quite large values, the Deborah number remains small. However, as the shear rate is increased further, the Deborah number reaches $\mathcal{O}(1)$ (and even larger) values, meaning that the time scale characteristic of deformation by the flow (i.e., $\dot{\gamma}^{-1}$) becomes comparable to (or smaller than) the relaxation time scale of the polymer, and viscoelastic effects become important. In this regime, as De is increased, the polydomain structure at first becomes increasingly refined, but eventually, at high enough shear rates, viscoelasticity appears to stabilize the system, the complex polydomain structure disappears and there is again the visual appearance of bands (this time oriented along the flow direction), followed at higher shear rates by what is apparently a monodomain structure (i.e., no birefringence). The latter series of transitions is the Deborah number cascade.

The numerical investigation presented here, together with the earlier study of Sgalari, Meiburg, and Leal,¹⁴ is a first step in the development of computational tools that can be used to simulate the behavior of nematic LCPs in flow using a specific molecular model for nematic LCPs.^{15,16} Before attempting more complex flows, it is important for us to first verify that the molecular theory is capable of predicting the onset and evolution of both types of disclinations (i.e., the *thicks* and *thins*) seen experimentally, and is capable of qualitatively reproducing the Ericksen and Deborah number cascades in a simple, two-dimensional shear cell. Several previous numerical investigations have considered the shear-flow behavior of nematic LCPs, using either molecular-based models^{17–19} or phenomenologically based tensor models^{20–23} that account for both the local and nonlocal contributions to the macroscopic stress (i.e., viscoelasticity and gradient elasticity). However, these studies have been limited to one- or two-dimensional flows between parallel plates wherein the flow is either held fixed (i.e., decoupled calculations) or coupled-flow calculations but with the polymer dynamics restricted to the shear plane. The calculations reported here consider the coupled-flow problem, in which the flow and polymer dynamics are coupled via the macroscopic stress, and are limited only in the sense that they assume *a priori* that there are no spatial gradients in the flow direction.

The neglect of spatial gradients along the flow direction is only strictly valid for two limiting cases: (i) low Er ($De \ll 1$), where the ratio between the streamwise and spanwise length scales emanating from the streamwise roll cells that are known to occur is very large (see, for example, Fig. 7 in Ref. 11); and (ii) “large” Deborah number, $De \geq 1$ ($Er \gg 1$), which is known from experiments to coincide with the reemergence of a banded pattern parallel to the flow direction. Given that (ii) simply corresponds to the Deborah number cascade, our simulations are not limited in this regard. With regard to (i), since we neglect streamwise gradients, we cannot predict the banded texture perpendicular to (and periodic along) the flow direction that is seen upon startup in experiments. Also, the disclinations predicted by the DMG model in these calculations must be interpreted as fully aligned with the flow and of infinite extent. Therefore, the model used in this investigation is inhibited from predicting three-dimensional disclination structures such as the closed-loop disclinations commonly observed in shear flow for both small-molecule liquid crystals²⁴ and LCPs.^{11,13} It is important to note that these limitations should *not* imply that the DMG model could not predict these phenomena via different boundary conditions²⁵ or a fully 3D calculation—it is simply unclear until such calculations have actually been done.

Previous theoretical and numerical predictions of the onset and growth of roll cells,^{26,27} and the resulting flow and orientation structures, in shearing flows of nematic polymers have been limited to the Leslie-Ericksen (LE) theory.^{28,29} Because the LE theory is known to exhibit gradient elasticity but no viscoelasticity, these predictions were therefore restricted to the study of the Ericksen number cascade, i.e., to the limiting case $De \rightarrow 0$. In a recent study, Feng, Tao, and Leal²⁷ carried out a numerical investigation of this cascade using the LE theory. Their results demonstrated the onset of the roll-cell formation, followed by destabilization of the roll cells, and finally the formation of ± 1 disclinations. An initial attempt to generalize these results by including viscoelastic effects via the DMG model was carried out by Sgalari, Leal, and Meiburg,¹⁴ following work by Feng, Sgalari, and Leal¹⁶ to derive the constitutive equation corresponding to the Marrucci-Greco extension of the Maier-Saupe Nematic potential.¹⁵ As was demonstrated by Feng *et al.*,¹⁶ in the limit $De \rightarrow 0$, the DMG theory reduces to the LE theory. Although the simulations of Sgalari *et al.* showed promise that the DMG model would capture the expected qualitative behavior for both the Ericksen and Deborah number cascades, numerical issues limited both the range of parameters studied and the accuracy of the simulations.

The present investigation extends the work of Sgalari *et al.*¹⁴ Improved numerical methods have allowed for more accurate solutions over a much wider range of parameters. However, though the velocity field is 3D in the sense that all three velocity components are nonzero, we have retained the *2D assumption* of no spatial gradients in the flow direction. In the present work, we show that computations carried out at low De do largely reproduce the results found by Feng *et al.*²⁷ using the LE model. More importantly, we show that the DMG model does produce both ± 1 and $\pm 1/2$ disclina-

tions for large Er and small, but nonzero, values of De . Furthermore, as De is increased, the flow is stabilized when viscoelastic effects become strong enough, just as expected qualitatively from the experimental observations of Larson and Mead.¹¹

II. THEORY AND NUMERICAL METHOD

A. The DMG model

The model used in this study is an extension, due to Marrucci and Greco¹⁵ and Feng *et al.*,¹⁶ of the molecular model first proposed by Doi,³⁰ which treats the LCP as a suspension of rigid rod-like molecules having an infinite length-to-width ratio. The forces acting on the rods are hydrodynamic, Brownian, and intermolecular forces. The dynamics of the system of rods is described in terms of an orientational distribution function $\psi(\mathbf{u}; \mathbf{r}, t)$, which gives the probability of finding a rod at position \mathbf{r} with an orientation, represented by the unit vector \mathbf{u} , within the solid angle $d\mathbf{u}$ at time t and is defined such that $\int_{S^2} \psi(\mathbf{u}; \mathbf{r}, t) d\mathbf{u} = 1$, where S^2 is the unit sphere in \mathbb{R}^3 .

If translational diffusion is neglected and the number density of the polymer molecules ν is assumed not to vary in space, the dynamic equation governing the distribution function ψ may be written as³¹

$$\frac{\partial \psi}{\partial t} + \mathbf{v} \cdot \nabla \psi = -\mathcal{R} \cdot (\mathbf{u} \times \boldsymbol{\kappa} \cdot \mathbf{u} \psi) + \bar{D}_r \mathcal{R} \cdot \left[\mathcal{R} \psi + \frac{\psi}{k_B T} \mathcal{R} \phi \right], \quad (1)$$

where \mathcal{R} is the rotational operator, $\mathcal{R} = \mathbf{u} \times (\partial / \partial \mathbf{u})$, which corresponds to the gradient operator in rotational diffusion,³² $\boldsymbol{\kappa} = (\nabla \mathbf{v})^T$ is the transpose of the velocity gradient, k_B is the Boltzmann constant, T is the absolute temperature, and ϕ is the mean-field nematic potential. Following Doi,³⁰ we use a pre-averaged approximation for the rotational diffusivity \bar{D}_r of the form

$$\bar{D}_r = \frac{D_r}{(1 - S^2)^2}, \quad (2)$$

where D_r is the rotational diffusivity for an isotropic solution having the same polymer concentration. $S = [(3\mathbf{A} : \mathbf{A} - 1)/2]^{1/2}$ is the scalar order parameter, where $\mathbf{A} = \int_{S^2} \psi \mathbf{u} \mathbf{u} d\mathbf{u} = \langle \mathbf{u} \mathbf{u} \rangle$ is the second moment of the distribution function. The colon represents the contraction operator, i.e., $\mathbf{A} : \mathbf{A} = A_{ij} A_{ji}$ with the summation convention, and $\mathbf{u} \mathbf{u}$ is the dyadic tensor product, i.e., $(\mathbf{u} \mathbf{u})_{ij} = u_i u_j$. In effect, Eq. (2) accounts for increased rotational diffusivity with increased local order.

The extended Doi theory (which we refer to here as the Doi-Marrucci-Greco theory) incorporates the Marrucci-Greco potential¹⁵ to account for nonlocal elastic contributions analogous to the Frank elasticity contributions of the Leslie-Ericksen theory; the mean-field molecular interaction proposed by Marrucci and Greco couples the Maier-Saupe excluded-volume potential^{33,34} to a nonlocal potential to account for long-range elastic interactions. The one-constant

approximation of the Marrucci-Greco potential, analogous to the $K_{11} = K_{22} = K_{33}$ approximation for the Leslie-Ericksen theory, is given by

$$\phi_{MG} = -\frac{3}{2} U k_B T \left(\mathbf{A} + \frac{\ell^2}{24} \nabla^2 \mathbf{A} \right) : \mathbf{u} \mathbf{u}, \quad (3)$$

where ℓ is the correlation length scale for the distortional elasticity interaction and U is a constant representing the strength of interactions between molecules.

As was proposed by Doi and Edwards,³¹ we represent the polymer stress $\boldsymbol{\tau}$ as the sum of a viscous stress $\boldsymbol{\tau}_v$ and an elastic stress $\boldsymbol{\tau}_e$. The viscous stress remains the same as in the original Doi theory because it is only a result of viscous friction. The more complicated elastic stress contribution, formulated by Feng *et al.*,¹⁶ may be written as

$$\boldsymbol{\tau}_e = 3 \nu k_B T \left\{ \mathbf{A} - U(\mathbf{A} \cdot \mathbf{A} - \mathbf{A} : \mathbf{Q}) - \frac{U \ell^2}{24} \left[\mathbf{A} \cdot \nabla^2 \mathbf{A} - \mathbf{Q} : \nabla^2 \mathbf{A} + \frac{\nabla \mathbf{A} : (\nabla \mathbf{A})^T - \nabla \nabla \mathbf{A} : \mathbf{A}}{4} \right] \right\}, \quad (4)$$

where $\mathbf{Q} = \int_{S^2} \psi \mathbf{u} \mathbf{u} \mathbf{u} \mathbf{u} d\mathbf{u} = \langle \mathbf{u} \mathbf{u} \mathbf{u} \mathbf{u} \rangle$ is the fourth moment of the distribution function and the contraction operations are defined as $\nabla \mathbf{A} : (\nabla \mathbf{A})^T = (\partial A_{kl} / \partial x_i) (\partial A_{lk} / \partial x_j)$ and $\nabla \nabla \mathbf{A} : \mathbf{A} = (\partial^2 A_{kl} / \partial x_i \partial x_j) A_{lk}$. The total stress is therefore

$$\boldsymbol{\tau} = \boldsymbol{\tau}_e + \frac{\beta}{(\nu L^3)^2} \left(\frac{\nu k_B T}{2 D_r} \right) \boldsymbol{\kappa} : \mathbf{Q}, \quad (5)$$

where $(\nu L^3)^2$ is the crowdedness factor and β is an $\mathcal{O}(10^3)$ constant.³¹

B. Closure approximation

Given that the stress tensor is only a function of the second and fourth moments of ψ (i.e., \mathbf{A} and \mathbf{Q} , respectively), we choose to make some mathematical simplifications in deriving a closed system of equations representing Eqs. (1), (4), and (5) in terms of \mathbf{A} . Following the Prager procedure,³⁵ we multiply Eq. (1) by $\mathbf{u} \mathbf{u}$ and integrate over configuration space (i.e., the surface of a unit sphere), to obtain a dynamic equation for the second moment tensor;

$$\frac{\partial \mathbf{A}}{\partial t} + \mathbf{v} \cdot \nabla \mathbf{A} = \boldsymbol{\kappa} \cdot \mathbf{A} + \mathbf{A} \cdot \boldsymbol{\kappa}^T - 2 \boldsymbol{\kappa} : \mathbf{Q} - 6 \bar{D}_r \left(\mathbf{A} - \frac{\mathbf{I}}{3} \right) + 6 \bar{D}_r U (\mathbf{A} \cdot \mathbf{A} - \mathbf{A} : \mathbf{Q}) + \frac{\bar{D}_r U \ell^2}{8} \times (\nabla^2 \mathbf{A} \cdot \mathbf{A} + \mathbf{A} \cdot \nabla^2 \mathbf{A} - 2 \nabla^2 \mathbf{A} : \mathbf{Q}), \quad (6)$$

where \mathbf{I} is the identity matrix. In order to obtain a closed system for \mathbf{A} , we approximate \mathbf{Q} as a function of \mathbf{A} . Such a closure expression yields a closed system of equations [i.e., Eqs. (4)–(6)] that can be coupled to the equations of motion to describe the dynamics of a nematic liquid polymer under an imposed flow.

In approximating \mathbf{Q} , we have chosen to use the so-called Bingham closure approximation.³⁶ Numerical investigations

by Feng *et al.*³⁷ suggest that the Bingham closure model is an appropriate choice in simulating complex flows. Because it is formulated using the simplifying assumption that the probability distribution function can be approximated in the form of a Bingham distribution, the Bingham closure model is only exact in the limit of weak flows where the viscous torque on molecules is not sufficient to skew the orientational distribution, i.e., in the limit of low De . This limitation results from the fact that the Bingham distribution is inherently restricted to a description of the orientational distribution that exhibits axial symmetry (i.e., uniaxial, biaxial, or triaxial symmetry). The model, therefore, cannot capture the shear-induced *wagging-to-flow-aligning* transition that is observed experimentally at high De .¹¹ Instead, the Bingham closure predicts a monotonic decrease in the wagging amplitude. But, given that tumbling, not wagging, is considered to be the source of disclinations and other defects in dynamic LCP systems, this deficiency in the Bingham closure does not inhibit its application in this context.

C. Governing equations

In making Eqs. (4)–(6) dimensionless, we take the relative velocity V between the shearing plates to be the characteristic velocity, and the plate separation H to be the characteristic length. For the flow considered here, the appropriate characteristic time is H/V . Based on this choice of characteristic scales, the dimensionless constitutive equation and equations of motion may be written as

$$\begin{aligned} \frac{\partial \mathbf{A}}{\partial t} + \mathbf{v} \cdot \nabla \mathbf{A} = \boldsymbol{\kappa} \cdot \mathbf{A} + \mathbf{A} \cdot \boldsymbol{\kappa}^T - 2\boldsymbol{\kappa} : \mathbf{Q} - \frac{f}{De} \left(\mathbf{A} - \frac{\delta}{3} \right) \\ + \frac{fU}{De} (\mathbf{A} \cdot \mathbf{A} - \mathbf{A} : \mathbf{Q}) + \frac{f}{2cS_{eq}^2} \frac{1}{Er} \\ \times (\nabla^2 \mathbf{A} \cdot \mathbf{A} + \mathbf{A} \cdot \nabla^2 \mathbf{A} - 2\nabla^2 \mathbf{A} : \mathbf{Q}), \end{aligned} \quad (7)$$

$$\text{Re} \left(\frac{\partial \mathbf{v}}{\partial t} + \mathbf{v} \cdot \nabla \mathbf{v} \right) = \nabla^2 \mathbf{v} - \nabla p + \nabla \cdot \boldsymbol{\tau}, \quad (8)$$

$$\nabla \cdot \mathbf{v} = 0, \quad (9)$$

where $f = 4/9(1 - \mathbf{A} : \mathbf{A})^{-2}$, $c = \nu k_B T / 2\eta D_r$ is the concentration parameter, and the nondimensional polymeric stress is given by

$$\begin{aligned} \boldsymbol{\tau} = \frac{c\beta}{(\nu L^3)^2} \boldsymbol{\kappa} : \mathbf{Q} + \frac{c}{De} [\mathbf{A} - U(\mathbf{A} \cdot \mathbf{A} - \mathbf{A} : \mathbf{Q})] \\ - \frac{1}{S_{eq}^2 Er} \left[\nabla^2 \mathbf{A} \cdot \mathbf{A} - \mathbf{Q} : \nabla^2 \mathbf{A} + \frac{\nabla \mathbf{A} : (\nabla \mathbf{A})^T - \nabla \nabla \mathbf{A} : \mathbf{A}}{4} \right]. \end{aligned} \quad (10)$$

The Reynolds number is defined as $\text{Re} = \rho V H / \eta$, with ρ and η being the density of the fluid and the constant solvent viscosity, respectively. Typically, $\text{Re} \sim 10^{-3} - 10^{-4}$ for systems similar to that which is considered here. We therefore use the Stokes form of the momentum equation, i.e., Eq. (8) with $\text{Re} = 0$.

The equilibrium value of the scalar order parameter S_{eq} is determined via substitution of the equilibrium (i.e., uniaxial) form for the second moment tensor

$$\mathbf{A}_{eq} = S_{eq} \left(\mathbf{nn} - \frac{\mathbf{I}}{3} \right) + \frac{\mathbf{I}}{3}, \quad (11)$$

with $\mathbf{n} = (1 \ 0 \ 0)^T$, into the steady, homogeneous form of Eq. (6).

The pressure and stress have been scaled by $\eta V / H$. Note that dimensional analysis yields two characteristic parameters. The first is the Deborah number De , defined as

$$De \equiv \frac{V/H}{6D_r}, \quad (12)$$

which is a ratio of the molecular relaxation time scale to the mean shear rate associated with the flow. The second is the Ericksen number Er , which represents the ratio of viscous stress to elastic stress,

$$Er \equiv \frac{\eta V H}{K} \left[= \left(\frac{24H^2}{cU\ell^2 S_{eq}^2} \right) \cdot De \right], \quad (13)$$

where $K = \frac{1}{8} \nu k_B T U \ell^2 S_{eq}^2$ is the elastic constant.¹⁵ We point out that although De appears explicitly in our expression for the Ericksen number, given the length scale dependence of Er (the length scale in this case being H), the two parameters can be varied independently.

D. Choice of parameter values

A number of the model parameters were held constant for this study, with the following values: $\beta = 1000$, $(\nu L^3)^2 = 2 \times 10^6$, $c = 100$, $U = 6$, and $\ell/H = 8.5 \times 10^{-3}$. The value used for the crowdedness parameter, $(\nu L^3)^2$, is typical of lyotropic systems. For a discussion of representative values of c , we refer the reader to the work of Feng and Leal.³⁸ In brief, c is proportional to the ratio of the zero-shear-rate viscosity of the LCP solution to the viscosity of the solvent. Reported values for c range from $\mathcal{O}(10^5)$ to $\mathcal{O}(10^6)$, depending on the solvent. However, since the polymeric stress scales with c , which contributes to the stiffness of the governing systems of equations, and because we consider Er and De spanning four decades, we use a more conservative value of 100 in this study. The value for the nematic strength parameter U was chosen so that the DMG model exhibited dynamics that are qualitatively consistent with the PBG solution used by Larson and Mead.¹¹ Larson and Mead reported that the PBG solution used in their investigations underwent a *tumbling-to-wagging* transition at $De \approx 2$, followed by a *wagging-to-flow-aligning* transition at $De \approx 5$. For the case of the unapproximated Doi theory,³⁰ which neglects gradient elasticity, $U = 6$ corresponds to these transition De values.³⁷ Since viscoelasticity is the primary driving force behind the dynamics of the model at high shear rates, where $Er \gg 1$ and $De > \mathcal{O}(1)$, we chose $U = 6$ for this investigation.

The nondimensional correlation length scale ℓ/H was chosen such that, for the parameter values given above, $Er/De = 1000$. Therefore, for the results presented here, the only parameters that were varied in the present study were Er and De . The ratio between the Ericksen and Deborah num-

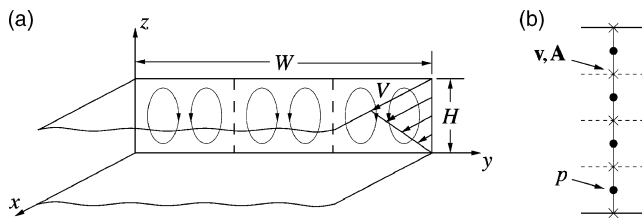


FIG. 1. Schematics of (a) the two-dimensional shear flow domain and (b) the staggered-grid layout along the z direction. The flow field is bounded along the spanwise direction by parallel plates separated a distance H and along the wall-normal direction by periodic boundaries separated a distance W . V is the relative velocity between the two plates. The velocity and configuration tensor are defined on the regular grid, while the pressure is defined at half-grid points.

bers in our calculations is approximately three orders of magnitude lower than the estimated value for the experimental systems. This choice of Er/De was primarily a consequence of computational limitations resulting from the fact that we consider Er (and De) values spanning nearly four decades and, although the parameters can be varied independently, chose to hold the ratio Er/De fixed. Holding the ratio Er/De fixed allows us to make direct comparison with the work of Larson and Mead,¹¹ wherein quantitative data were collected over a range of shear rates for two different gap widths. But, given that we only vary Er in our calculations, the largest allowable value for Er/De is one for which the solution can be adequately resolved for the largest Er considered in this study ($Er=15000$). Hence, $Er/De=1000$ used in our simulations was determined using refinement studies. A potential consequence of using a relatively low Er/De is the inability to sufficiently separate the two distinct contributions to the polymeric stress: gradient elasticity, the driving force behind the Ericksen number cascade; and viscoelasticity, which stabilizes the system during the Deborah number cascade. In turn, we would be unable to sufficiently resolve the two regimes. This, however, does not seem to be the case for the calculations discussed here.

E. Discretization

As depicted in Fig. 1(a), the computational domain is a rectangular region lying within a plane orthogonal to the primary flow direction (i.e., the y, z plane) bounded by two parallel plates at $z=0, 1$ and periodic boundaries at $y=0, W/H$. The relative velocity between the plates is given as V , and, as previously stated, the characteristic length is taken as H . The domain is discretized in y , the spanwise direction, using a uniform grid spacing h . To cluster grid points near the upper and lower domain boundaries, we utilize the coordinate transformation³⁹

$$z_k = \frac{1}{2} \left\{ 1 + \frac{\tanh \left[\delta \left(\xi_k - \frac{1}{2} \right) \right]}{\tanh(\delta/2)} \right\}, \quad (14)$$

where $\xi_k = \frac{k-1}{N_z-1}$, $k=1, \dots, N_z$, to generate a nonuniform grid in z , the wall-normal direction. A value $\delta=2.0$ was used for the results presented in this work. A staggered grid is used,

with respect to the z direction [see Fig. 1(b)], such that the components of \mathbf{v} and \mathbf{A} are defined on the regular mesh, with N_z nodes, and the N_z-1 pressure nodes are staggered at half-grid points. The continuity constraint is enforced at the p nodes, while the equations of motion and evolution equation for the polymer configuration are solved at the (\mathbf{v}, \mathbf{A}) nodes.

As the texture length scale decreases with increasing values of the Ericksen number Er , the results presented in Sec. III were obtained using grid spacings ranging from $h=1/32$ to $1/1024$, where $h=\Delta_y=\Delta_\xi$. The mesh was refined until there was no discernible difference in either the transient structure or the time scales associated with the onset of the initial roll cell instability and the ensuing director dynamics for a given initial configuration. An adequate domain width was chosen in a similar manner, with the additional constraint that the aspect ratio of the steady-state or transient roll cells not vary beyond a given value of W/H .

To reduce the size of the numerical problem, albeit the flow is still three-dimensional in the sense that all three components of \mathbf{v} are nonzero and we consider the general form for \mathbf{A} at each point, we assume that there are no gradients in the streamwise direction x . Given the periodic boundary conditions imposed at $y=0, W/H$, we use spectral collocation for the flow and configuration components in the spanwise direction. Derivatives with respect to the y direction are therefore evaluated efficiently via the fast Fourier transform. Wall-normal derivatives are evaluated using a second-order finite-difference formulation. The steady-Stokes form of Eq. (8) is solved using the Uzawa biconjugate gradient stabilized⁴⁰ method, the details of which are presented in a previous paper.⁴¹ We integrate the evolution equation for the polymer configuration (7) using the second-order Runge-Kutta TVD scheme proposed by Shu and Osher.⁴²

F. Boundary and initial conditions

No-slip conditions are imposed on the velocity components at $z=0, 1$, i.e., $\mathbf{v}_{z=0,1}=(v_x \ v_y \ v_z)^T=(z \ 0 \ 0)^T$. With regard to boundary conditions for the configuration tensor \mathbf{A} , the polymer configuration is *anchored* along the upper and lower boundaries of the domain such that the \mathbf{A} remains fixed in its uniaxial form [i.e., Eq. (11), with $\mathbf{n}=(0 \ 1 \ 0)^T$]. Initial conditions for the velocity components are those of linear shear flow, where $\mathbf{v}(\mathbf{x}, t=0)=(z \ 0 \ 0)^T$. A random-phase perturbation, with an $\mathcal{O}(10^{-6})$ amplitude, is introduced into the polymer configuration, which is initially defined such that the mean orientation is along the y direction. These boundary conditions are consistent with both the LE theory analyses^{27,26} and experiments of Larson and Mead.^{10,11} Given an initial orientation along the y axis, these studies found the earliest-observed instability to be roll cells accompanied by birefringent stripes oriented along the flow direction. If the initial mean orientation is along either the velocity gradient or flow directions, Larson and Mead reported that the earliest instability observed was the formation of a banded pattern oriented along the y axis and periodic along the flow direction, followed at somewhat later times by the roll-cell instability in the flow direction. As previously mentioned in Sec. I, since we neglect streamwise gradients in this

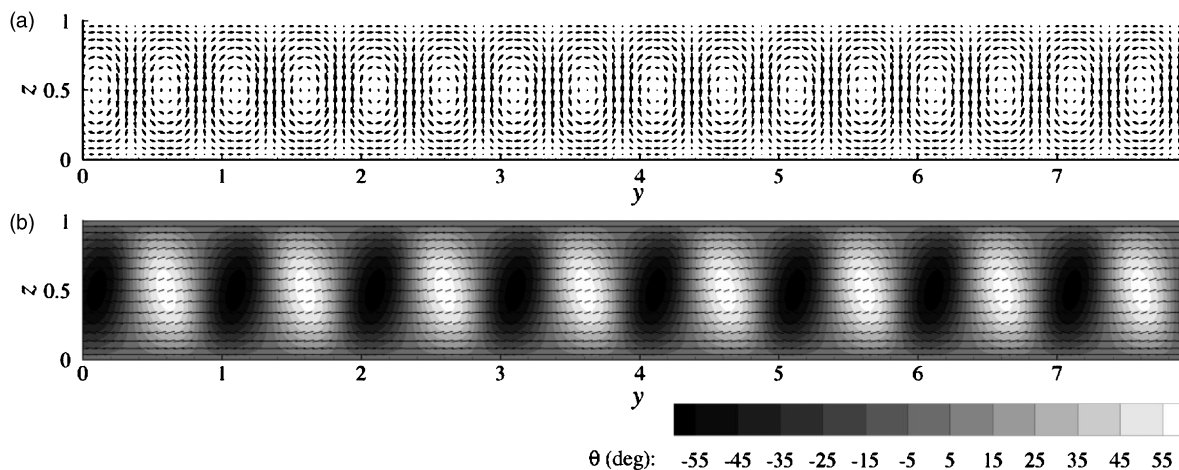


FIG. 2. Steady-state (a) secondary flow vector field (v_y, v_z) and (b) director vector field $\mathbf{d}(\mathbf{x})$ and tip angle θ scalar contour for $Er=50$ ($De=0.05$). Note: a color animation showing the evolution of the system to this final state is available online.

study, even with the consideration of an initial orientation along the velocity gradient or flow directions, our simulations cannot capture the initial spanwise-oriented banded pattern.

III. RESULTS AND DISCUSSION

We have found that the DMG model exhibits dynamics that are in qualitative agreement with both experimental^{10,11} and applicable theoretical and numerical investigations.^{26,27,43} As mentioned earlier, the only parameters varied in our calculations are De and Er . Given that the ratio Er/De is held constant, reference will primarily be made to changes in the Ericksen number for the results presented here. In the context of the LE theory, the average orientation, referred to as the director, is described using the unit pseudovector \mathbf{n} , i.e., \mathbf{n} and $-\mathbf{n}$ are energetically equivalent. For the DMG theory, the average orientation can be associated with the eigenvector representative of the largest eigenvalue of \mathbf{A} . To distinguish this difference between the two different models, we describe the director using the unit pseudovector \mathbf{d} .

A. Low to moderate shear rates, $Er \lesssim 6000$ ($De \lesssim 6$)

For the case of low to moderate shear rates, the polymer and coupled fluid dynamics are primarily a function of the contribution of gradient elasticity to the macroscopic stress. Arguably, the effects of viscoelasticity are non-negligible as De approaches and exceeds unity, but our results indicate that the system dynamics and resulting structure are dominated by the so-called Frank stress. For finite Er less than approximately 6000 ($De \lesssim 6$), the responses of the perturbed system, in order of increasing Er , were as follows:

1. Stable simple shear,
2. stable roll cells, and
3. irregular structure accompanied by disclination formation.

Due to computational limitations, the range of Er listed for each regime in the sections that follow has an associated error of approximately 10%.

1. Stable simple shear, $Er \lesssim 40$

For Ericksen values less than approximately 40, the system exhibits stable simple shear with the average polymer orientation along the spanwise direction, generally referred as to the *log-rolling* configuration, throughout the flow domain. Although there is an initial transient regime, during which the director precesses about the y axis, the amplitude of these rotations slowly decreases over time as $\mathbf{d} \rightarrow (0 \ 1 \ 0)^T$.

2. Stable roll cells, $40 \lesssim Er \lesssim 250$

With increasing shear rate, the log-rolling configuration observed at lower Er is no longer stable, and the numerical perturbation introduced into the configuration field at the beginning of the simulation gives rise to the formation of roll cells via a mechanism associated with anisotropy of the viscous stress for a sheared nematic.⁴⁴ The resulting flow structure is paired, counter-rotating vortices oriented along the flow direction, and the director exhibits modulation in its orientation, with respect to the computational plane (i.e., the y - z plane), along the spanwise direction. An example of the stable flow and orientation configurations, for $Er=50$, is presented in Fig. 2. The angle between the director and the y - z plane, which we refer to here as the tip angle, is given as θ . For $Er=50$, the (height-to-width) aspect ratio of the steady-state roll-cell structure is $AR=2.0$, and the maximum value of the steady-state secondary flow, relative to the primary flow, is 0.012. The largest deviation of the director from the computational plane $|\theta|_{\max}$ of approximately 60 degrees occurs at the centers of the roll cells, where the magnitude of the vorticity associated with the secondary flow reaches a maximum. The evolution of the director orientation \mathbf{d} , as a function of strain units τ , within the center of a roll cell [at $(y, z) = (4.62, 0.5)$ in Fig. 2] is presented in Fig. 3. As was observed in the LE calculations of Feng *et al.*,²⁷ a log-log plot of the data presented in Fig. 3 shows that the growth of the instability is exponential at the outset, but becomes linear at a given strain, prior to reaching steady state. For $Er=50$,

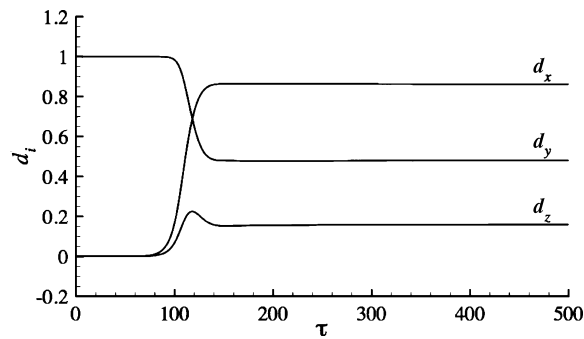


FIG. 3. Evolution of director components at $(y, z) = (4.62, 0.5)$, for $Er = 50$ ($De = 0.05$).

this transition in the growth rate occurs at $\tau \approx 80$ strain units, and steady state is reached at $\tau \approx 160$ strain units.

With regard to their low shear rate results for an initial orientation along the spanwise direction, Larson and Mead¹¹ reported that a critical shear rate exists for which, after prolonged shearing, a banded texture appears in the form of birefringent stripes oriented along the flow direction; the banded texture undergoes refinement until it reaches a steady-state spacing in 30–100 strain units; and there is a monotonic decrease in the stripe spacing with increasing Er . Using polarizing microscopy, Larson and Mead found the banded texture to result from a periodic tipping of the mean orientation away from the y direction, into and out of the plane orthogonal to the flow direction (the y - z plane in our calculations). In accordance with these experimental observations and the LE model predictions reported by Feng *et al.*,²⁷ we found that as the Ericksen number was increased, there was a corresponding increase in the aspect ratio of the resulting roll cells ($1.75 \leq AR \leq 3.50$); the director rotates further away from the computational plane within roll-cell vortices ($50 \leq \theta_{\max} \leq 75$ degrees); and there is an increase in the rate at which roll cells form. Additionally, the director configuration observed by Larson and Mead is precisely that which was predicted by both the DMG theory in our calcu-

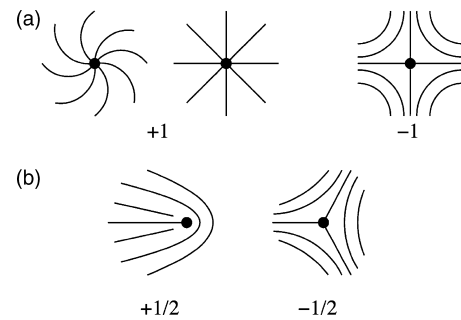


FIG. 4. Schematics of (a) 1-strength and (b) 1/2-strength disclinations observed in calculations. The dot represents the defect core, and the lines are the director vector field lines (i.e., lines drawn tangent to the vector field) projected onto the computational domain. The strength and sign correspond to the relative rotation of the director around a path encircling the disclination.

lations and the LE theory in Larson's linear stability analysis,²⁶ the earlier analysis of Manneville and Dubois-Violette,⁴³ and the simulations performed by Feng *et al.*

Quantitatively, the most relevant data for direct comparisons to experiment and the LE calculations are the critical Er at which the system is unstable to roll-cell formation and the scaling of the roll-cell aspect ratio as a function of Er . As the material constants for the PBG solutions used by Larson and Mead^{10,11} are not known, we are unable to compare the critical Er prediction of the DMG model with experimental data. However, using the Leslie-Ericksen limiting form of the polymeric stress¹⁶ and $\alpha_4/2$ as the characteristic viscosity, we determined the Leslie viscosities for our calculations to be $(\alpha_1, \alpha_2, \alpha_3, \alpha_5, \alpha_6) = (-10.8, -20.6, 0.765, 17.3, -2.58)$, which are of the order of those of the "typical nematic polymer" used in Larson's analysis of the LE theory²⁶ and the simulations of Feng *et al.*²⁷ It is, therefore, not surprising that the critical Er at which the perturbed system is unstable to roll-cell formation, $Er \approx 40$, is comparable to the values reported by Larson and Feng *et al.* Since pertinent data are still

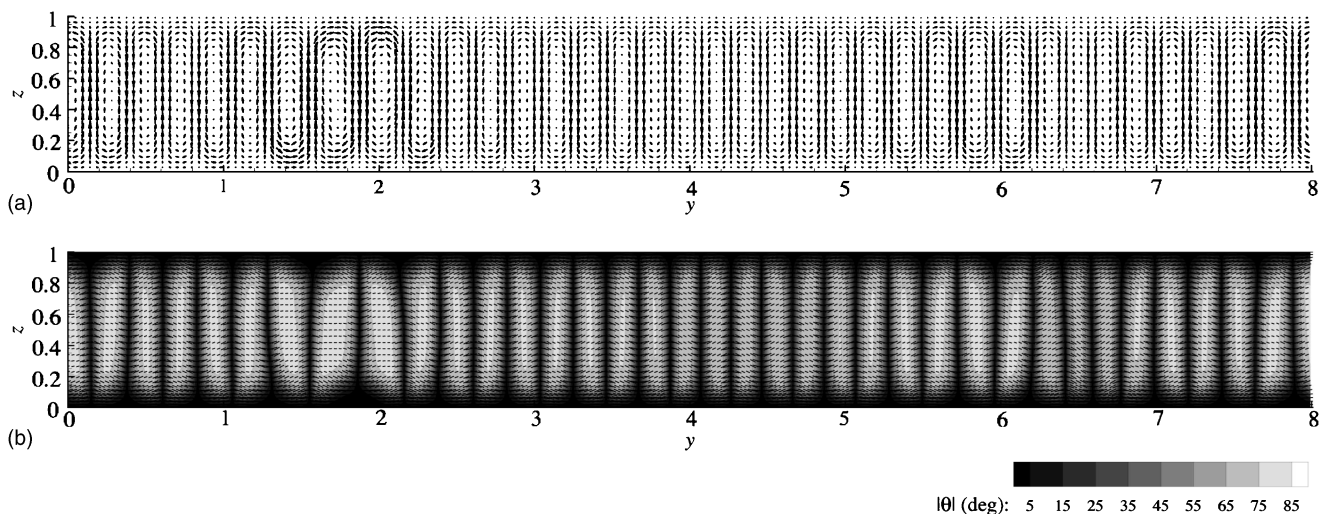


FIG. 5. (a) Secondary flow vector field (v_y, v_z) and (b) director vector field $\mathbf{d}(\mathbf{x})$ and tip angle magnitude $|\theta|$ scalar contour for $Er = 500$ ($De = 0.5$) at $\tau = 35$ strain units.

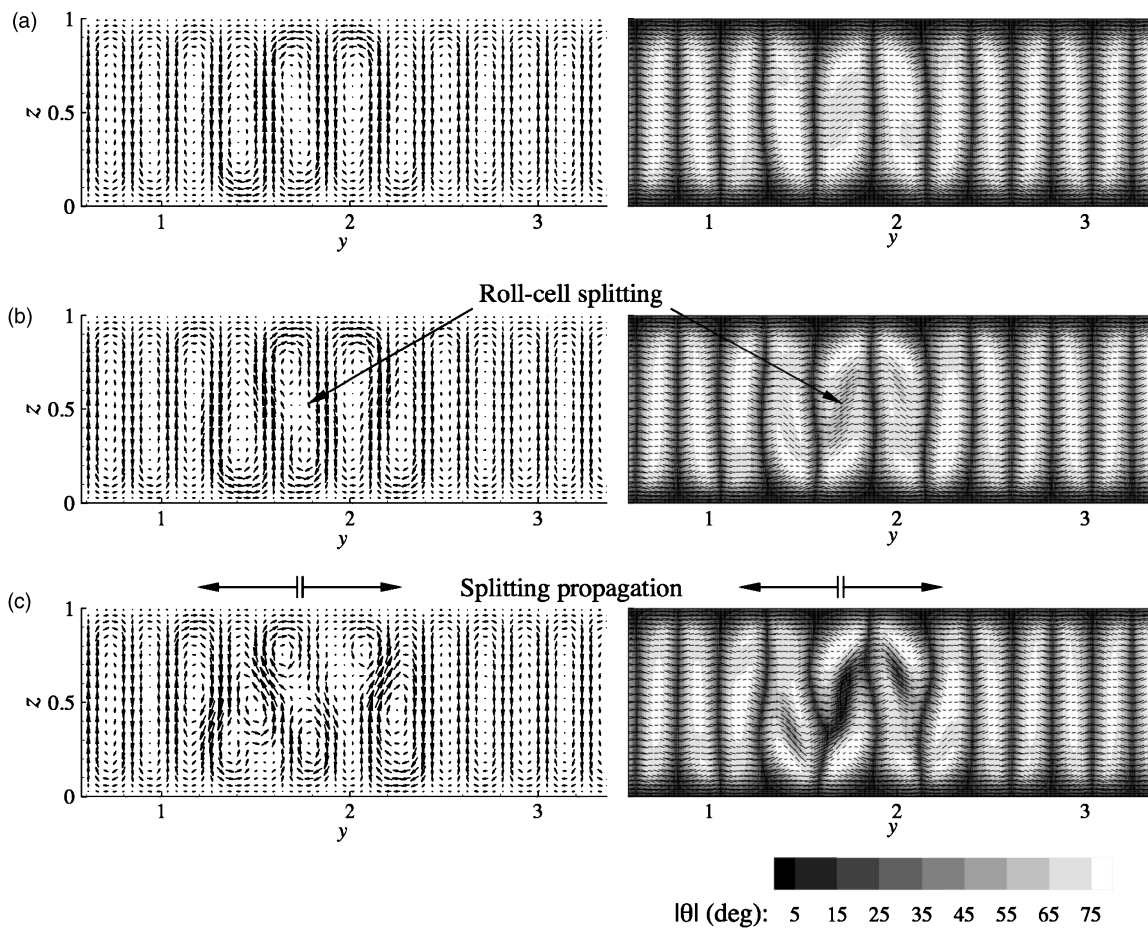


FIG. 6. Roll-cell splitting and propagation for $Er=500$ ($De=0.5$). (left) Secondary flow vector field (v_y, v_z) and (right) director vector field $\mathbf{d}(\mathbf{x})$ and tip angle magnitude $|\theta|$ scalar contour at (a) $\tau=40$, (b) $\tau=45$, and (c) $\tau=50$ strain units. Note: a color animation showing the splitting process within the region shown here is available online.

to be presented in the next two sections, we will postpone our discussion of the scaling behavior of AR in our simulations and comparison of the DMG model predictions to those of the LE theory and Larson and Mead's experimental data until the end of Sec. III A.

3. Irregular flow and orientation structure accompanied by disclination formation, $250 \lesssim Er \lesssim 6000$

For Er greater than approximately 250, the regularity of the structure observed for lower Er , where a single mode (i.e., roll cells with a single aspect ratio) persists for an indefinite period of time, yields to the intrinsic nonlinearity of the model and the decrease in the elastic contribution to the stress relative to the viscous stress. As the mean orientation within the roll-cell vortices tips further toward the flow direction with increasing Er , gradient elasticity can no longer inhibit the temporal modulations, in the form of either wagging or tumbling. These local fluctuations in the director field lead to a breakdown of the regular roll-cell structure via a mechanism we refer to here as *roll-cell splitting*, where smaller “daughter cells” form as adjacent roll cells split along the z direction. Given sufficiently high Er values, the resulting irregular flow structure and its propagation throughout the domain are accompanied by the formation of 1/2- and

1-strength orientational defects, depictions of which are presented in Fig. 4. As ± 1 disclinations were obtained by Feng *et al.* using the LE model,²⁷ and given the fact that the DMG model reduces to the LE model in the limit as $De \rightarrow 0$, we “expect” to observe ± 1 disclinations with the DMG model. Disclinations of strength 1/2, however, have not previously been predicted in coupled-flow simulations.

As is the case for lower Er (i.e., $40 \lesssim Er \lesssim 250$), the initial structure observed for Er within this regime is roll cells. The distinct difference between this initial *transient* structure and the *steady-state* structure observed at lower Er is that there is not a single roll-cell aspect ratio observed, but a narrow distribution of aspect ratios. As a typical example of the initial roll-cell structure seen within this regime, we present the flow and orientation configurations for $Er=500$ at $\tau=35$ strain units in Fig. 5; the dark vertical strips in Fig. 5(b) correspond to the region where the tip angle $|\theta| \rightarrow 0$ between adjacent roll cells. The maximum secondary flow velocity, relative to the imposed boundary velocity, is 0.014, and the largest deviation of the director from the computational plane $|\theta|_{\max}$ is 78.7 degrees. Although most roll cells within the domain have an aspect ratio of approximately 5, it is evident that $3.13 \leq AR \leq 5.88$. With increased strain, as can be seen in the series of snapshots of the secondary velocity and director fields shown in Fig. 6, the cells having the

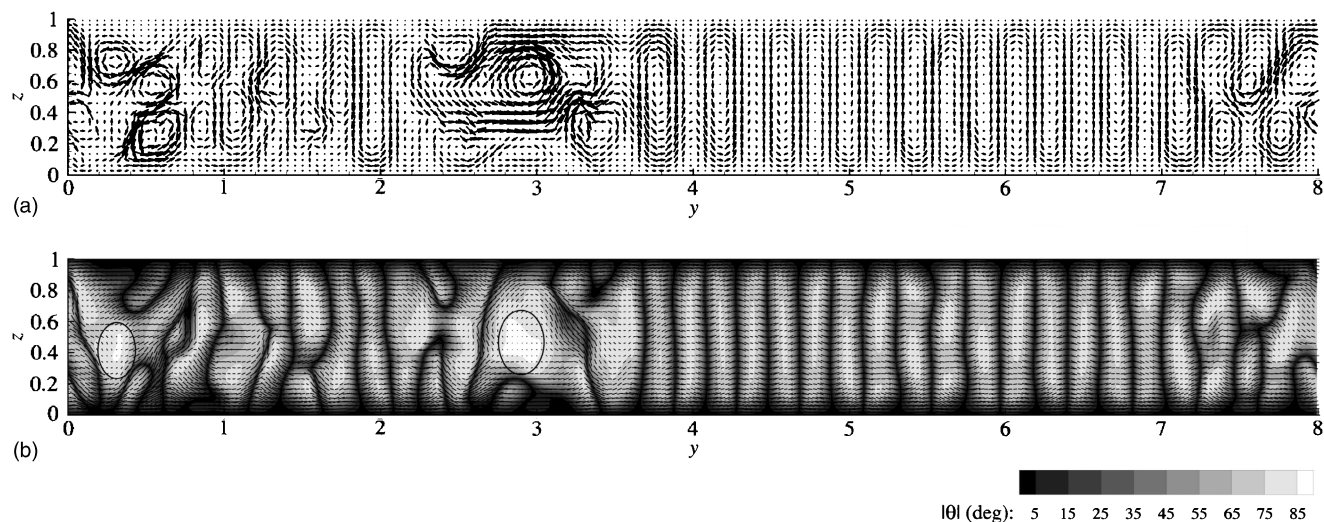


FIG. 7. (a) Secondary flow vector field (v_y, v_z) and (b) director vector field $\mathbf{d}(\mathbf{x})$ and tip angle magnitude $|\theta|$ scalar contour for $Er=500$ ($De=0.5$) at $\tau=143$ strain units, just prior to the formation of the first ± 1 defect pair.

smallest aspect ratio (between $1.56 < y < 2.16$ in Figs. 5 and 6) undergo splitting at $\tau \approx 40$. The instability and corresponding perturbation in the orientation field then propagate to the left and right [see Fig. 6(c)] as once-stable roll cells and daughter cells formed earlier in the process split to produce vortices of various sizes and strengths.

As the instability initiated by roll-cell splitting propagates throughout the computational domain, the irregularity of the flow and orientation structure gives rise to the forma-

tion of disclinations. For $Er \leq 700$, we observed only the formation of ± 1 disclination pairs, which are formed by the same “ridge-splitting” mechanism first identified in simulations using the Leslie-Ericksen model by Feng *et al.*²⁷ During this process, localized ridges form within the director field, along which the director is oriented primarily in the flow direction. Given the proper conditions, with regard to the flow and director fields, the ridge splits to form a ± 1 pair of disclinations in what is referred to as the *escaped configu-*

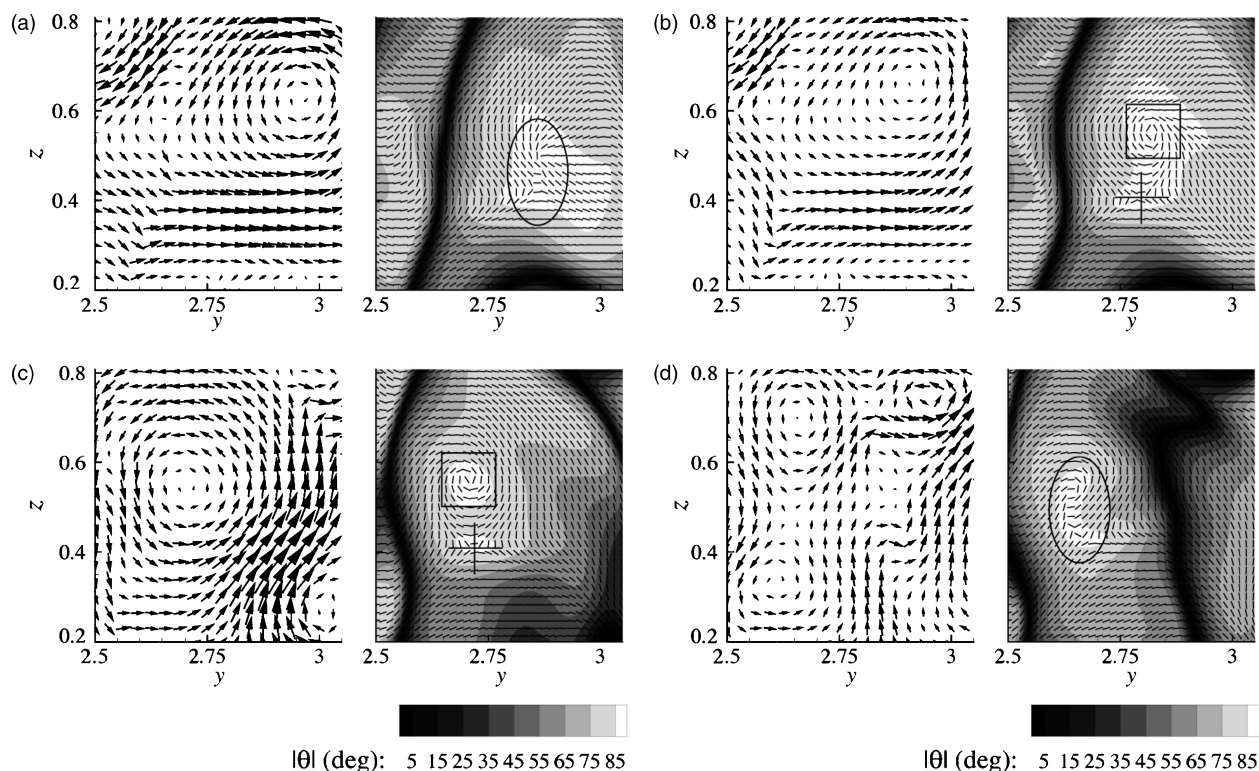


FIG. 8. Initial disclination formation for $Er=500$ ($De=0.5$). (left) Secondary flow vector field (v_y, v_z) and (right) director vector field $\mathbf{d}(\mathbf{x})$ and tip angle magnitude $|\theta|$ scalar contour at (a) $\tau=143$, (b) $\tau=145$, (c) $\tau=150$, and (d) $\tau=154$ strain units. The ellipses highlight the “ridge” structures from which the ± 1 defect pair originates (a) and, at a later time, annihilates via recombination (d). Crosses and squares indicate -1 and $+1$ disclinations, respectively. Note: a color animation showing the dynamics of flow and director fields depicted in this sequence of images is available online.

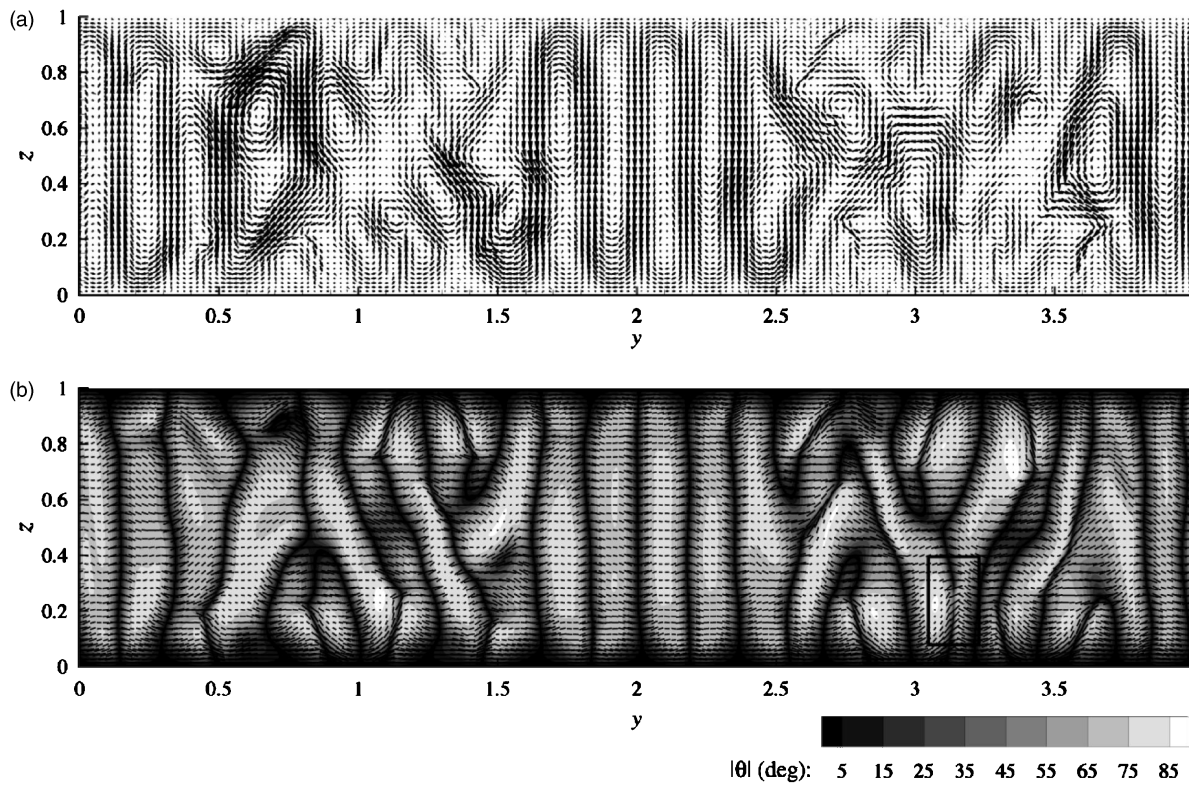


FIG. 9. (a) Secondary flow vector field (v_y, v_z) and (b) director vector field $\mathbf{d}(\mathbf{x})$ and tip angle magnitude $|\theta|$ scalar contour for $Er=1000$ ($De=1$) at $\tau=60$ strain units. Note: a color animation showing the evolution of the flow and microstructure representative of the data presented here is available online.

ration, wherein these disclinations have “escaped” a true orientational singularity by rotating at their core into the flow direction without any change in the degree of alignment. As an example of the flow and microstructure just prior to the formation of a ± 1 disclination pair, we show a snapshot of the secondary flow and director fields for our $Er=500$ calculation at $\tau=143$ strain units (the approximate time at which the first defects were observed in this simulation) in Fig. 7. The ellipses in Fig. 7(b) indicate regions containing the aforementioned ridge configurations, as indicated by the shrinking of the director field vector to a point in the ellipse centers and the associated transition in the overlaid $|\theta|$ contour from white along the ridge, where $|\theta| \approx 90$ degrees, to darkening shades of gray, indicating a decrease in $|\theta|$, away from the ridge. As alluded to above, the ridge structure does not always lead to the development of disclinations. The highlighted ridge at $y \approx 2.9$ in Fig. 7(b) leads to the formation of a ± 1 pair of defects, the details of which will be discussed below, while the ridge at $y \approx 0.3$ is gone within a few strain units as the local orientation assumes that of the surrounding field.

The series of snapshots presented in Fig. 8 shows the evolution of the flow and director fields during the formation and subsequent annihilation of the first-observed disclinations for the $Er=500$ results. (The reader should note that director field vectors in Fig. 8 have been plotted with a fixed length, rather than their projected length in the y - z plane as in previous figures, so as to emphasize the defect structure.) As previously mentioned, the formation of ± 1 disclinations is initiated by the appearance of a ridge structure [high-

lighted in the director field plot in Fig. 8(a) by an ellipse] at $\tau \approx 143$ strain units. At $\tau \approx 145$ strain units, the ridge splits to form a ± 1 pair of disclinations, as we can see by comparing the director field in the right plot of Fig. 8(b) to the disclination depictions presented in Fig. 4(a). Upon formation, the disclinations move through the domain [Fig. 8(c)] via convection, and after a given amount of time, which ranged from 10 to 20 strain units for the results presented here, the oppositely signed disclinations annihilate one another by recombining at $\tau \approx 154$ strain units [Fig. 8(d)]. In this example, it appears that since a large degree of tipping (which possibly aids in the formation of the ridge structure) occurs at the cell core, the disclination structure is a direct result of the relatively high-strength vortex encompassing the region in which the disclination pair resides. There is also a noticeable synchronization between the flow and configuration fields as the disclinations and encompassing roll cell propagate along the spanwise direction within the domain, and the splitting of the large roll cell occurs at approximately the same strain at which the disclinations recombine. Although this coupling between the flow and disclination dynamics, in which ± 1 disclination pairs originate in the core of relatively high-strength roll cells, is quite common in this regime, we have also observed defect formation via ridge-splitting in regions bridging several vortices and in the regions between adjacent vortices.

For $Er \geq 700$, we observed the formation of both ± 1 and $\pm 1/2$ disclination pairs. As was the case for lower Er , where we observed only ± 1 disclinations, the initial structure is roll cells. This is followed by the breakdown of the regular roll-

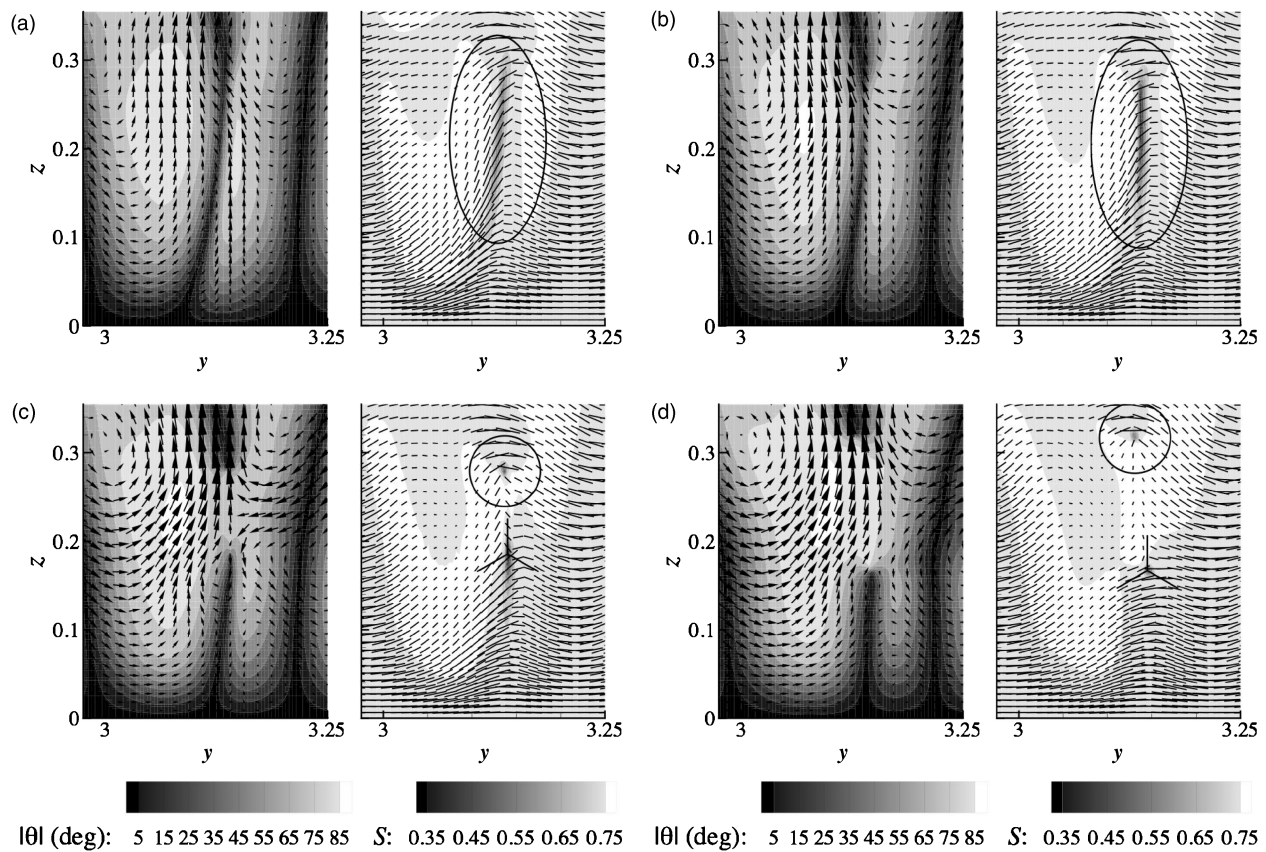


FIG. 10. Disclination formation for $Er=1000$ ($De=1$). (left) Secondary flow vector field (v_y, v_z) and tip angle magnitude $|\theta|$ scalar contour and (right) director vector field $\mathbf{d}(\mathbf{x})$ and order parameter S scalar contour at (a) $\tau=58$, (b) $\tau=60$, (c) $\tau=61$, and (d) $\tau=63$ strain units. The three-armed symbols and circles in (c) and (d) indicate the $-1/2$ and $+1/2$ disclinations, respectively. Note: a color animation of the system dynamics depicted in the sequence of images presented here is available online.

cell structure via the splitting instability at a strain that decreases with increasing Er . However, in this case, as the roll-cell splitting instability propagates throughout the domain, in addition to ± 1 defect pairs generated via the ridge-splitting mechanism, we observe $+1/2$ and $-1/2$ disclinations. As an example of the flow and microstructure during the formation of a pair of $\pm 1/2$ defects, we show the secondary flow and director fields for $Er=1000$ at $\tau=60$ strain units in Fig. 9, the strain at which we first observe $1/2$ -strength defects during this simulation. The respective maxima in the secondary velocity and tip angle magnitude are $|\mathbf{v}|_{\text{sec}}=0.015$ and $|\theta|=90$ degrees. The region in which we observed the $\pm 1/2$ pair of disclinations is indicated by a rectangle in the lower right corner of Fig. 9(b).

The details of the mechanism by which $\pm 1/2$ disclination pairs form can be discerned from Fig. 10, in which we show an example of the evolution of the secondary flow and director and order parameter fields during disclination formation from our $Er=1000$ simulation. At $\tau \approx 58$ strain units [Fig. 10(a)], a localized twist develops in the director field, originating at approximately $(y, z)=(3.14, 0.22)$ (the region indicated by the ellipse). This is accompanied by a reduction in the local order parameter S from the equilibrium value of 0.74 to a minimum value of 0.54. At $\tau=60$ strain units, curvature (i.e., twist) in the director field $\partial^2 \theta / \partial z^2$ along $y=3.14$ continues to increase, as indicated by the narrowing

of the dark band in the $|\theta|$ contour in the left plot in Fig. 10(b), and the continued strain results in a further reduction in the local minimum value of S to 0.43. As the amount of stored elastic energy $K \partial^2 \theta / \partial z^2$ increases, the localized region becomes susceptible to an instability that lowers the distortional energy at the expense of the energy required for the creation of a defect; specifically, for this case, a $\pm 1/2$ disclination pair that forms just after Fig. 10(b). Following the formation of the defect pair, S reaches local minimum values of 0.34 and 0.25, respectively, at the cores of the $+1/2$ and $-1/2$ disclinations [which can be identified by comparison of the highlighted regions in the director field shown in Fig. 4(b)]. It may be noted that there is an abrupt change in the director orientation along $y=3.1$ at the core of each disclination where the director goes from being oriented along the y direction above and below the disclination pair to a nearly flow-aligning orientation between them. There is also a noticeable perturbation in the secondary flow field in the vicinity of the $+1/2$ disclination and increase in $\partial v_z / \partial z$ between the two defects as the $+1/2$ disclination moves upwards toward the center of the domain while the $-1/2$ disclination remains stationary. These transitions in the director orientation and changes in the flow brought about by the

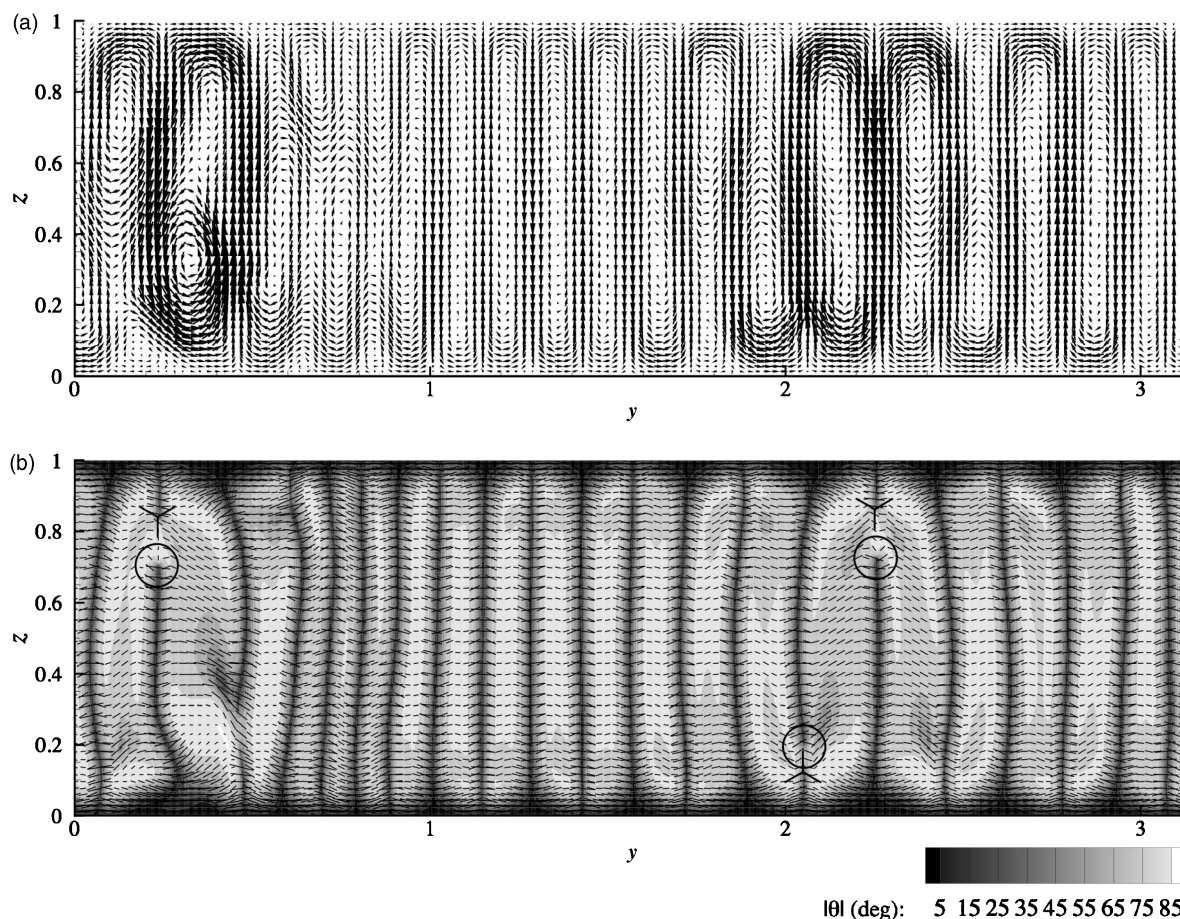


FIG. 11. (a) Secondary flow vector field (v_y, v_z) and (b) director vector field $\mathbf{d}(\mathbf{x})$ and tip angle magnitude $|\theta|$ at $\tau=39$ strain units for $Er=2000$. The three-armed symbols and circles indicate the $-1/2$ and $+1/2$ disclinations, respectively. Note: a color animation showing the evolution of the flow and microstructure is available online.

strong coupling between the flow and microstructure become more pronounced upon formation of the final defect structure [Fig. 10(d)].

For $Er \geq 1500$, we observed the formation of ± 1 and $\pm 1/2$ disclinations *prior* to the breakdown of the initial roll-cell structure. For $1500 \leq Er \leq 4500$, the defect structures observed at the earliest time (i.e., the least amount of strain) are $\pm 1/2$ disclinations that form near the upper and lower domain boundaries in the convergent region between adjacent roll cells. A typical example of a solution exhibiting such a structure is presented in Fig. 11, wherein we show a snapshot of the velocity and director fields for $Er=2000$ at $\tau=39$ strain units. Referring to Fig. 11(a), one can see that, although some vortices have undergone splitting, the overall roll-cell structure remains relatively intact. In considering the magnitude of the tip angle $|\theta|$, the director orientation is primarily along the flow direction within the roll cells, where $|\theta| \approx 80$ degrees, but is subject to large gradients along the spanwise direction between adjacent cells, where $|\theta| \rightarrow 0$. In convergent regions near the upper and lower boundaries of the domain, there is an increase in the curvature of the director field with increased strain as was observed at lower Er . As before, these localized regions become susceptible to an instability that lowers the distortional energy at the expense of the energy required for the creation of a $\pm 1/2$ pair of

disclinations. In this case, however, the $-1/2$ disclination remains stationary near the wall as the $+1/2$ moves toward the center of the domain between the adjacent roll cells. At large strain, we also observe ± 1 defect pairs which form via the ridge-splitting mechanism and exhibit dynamics that do not differ, qualitatively, from those seen in solutions for lower Er .

For $4500 \leq Er \leq 6000$ within this regime, although the first-observed defect structure is still $\pm 1/2$ defect pairs, which form near the upper and lower domain boundaries, the low-order cores from which the defects originate are not localized to small regions, but, rather, span the entire gap height between adjacent roll cells. This results in stationary $1/2$ -strength defects, of alternating sign, along the upper and lower domain boundaries. As was observed for lower Er values, upon formation of the $\pm 1/2$ pair of disclinations, the director orientation between the defects assumes an orientation that coincides with the flow axis, thereby forming ridges that extend across the entire gap height between adjacent roll cells, wherein the tipping angle magnitude $|\theta|$ modulates between approximately 90 degrees at the ridge “peaks” and 75 degrees in the cores of roll cells along the y direction. With increased strain, ± 1 defects emanate from either end of the ridges as a result of the same *ridge-splitting* mechanism observed at much lower Er values. In Fig. 12, we show a snap-

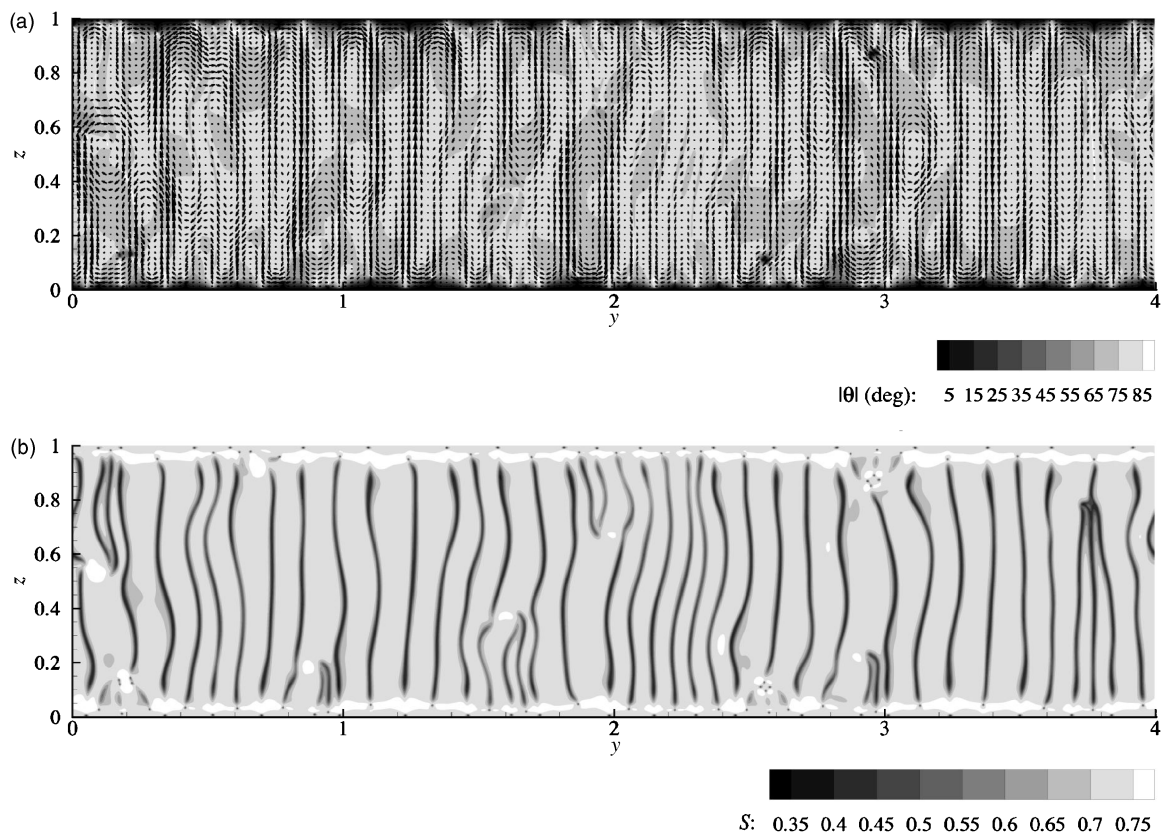


FIG. 12. (a) Secondary flow vector field (v_y, v_z) and tip angle magnitude $|\theta|$ scalar contour and (b) order parameter S scalar contour for $Er=5000$ ($De=5$) at $\tau=28$ strain units. Note: a color animation showing the evolution of the flow and microstructure is available online.

shot of the secondary velocity, tip angle magnitude, and order parameter fields for $Er=5000$ at $\tau=28$ strain units, just following formation of the initial $\pm 1/2$ defects [as is evident from the small dark dots along the upper and lower bounds of the domain in Fig. 12(b)] and prior to the formation of the first-observed ± 1 disclination pairs. Although many vortices have undergone splitting, the overall roll-cell structure initially remains intact [see Fig. 12(a)]. The maximum secondary flow velocity, relative to the base flow, is 0.011, $|\theta|_{\max}=90$ degrees, and $0.34 \leq S \leq 0.78$. The ridges from which ± 1 disclination pairs are continually produced coincide with the low-order bands that span the height of the gap in Fig. 12(b), wherein S drops from its equilibrium value of 0.74 to approximately 0.43.

In Fig. 13, we present an example of the dynamics of the flow and director fields during the formation of the initial $\pm 1/2$ defect pair and subsequent production of the ± 1 defect pairs between adjacent roll cells. In comparing Figs. 13(a) and 13(b), we see that the initial structure observed is roll cells and a modulation in the director field about the computational plane along the y direction [Fig. 13(a)]. The dark stripes along $y=0.53, 0.61,$ and 0.70 in the order parameter contour in Fig. 13(a) highlight the low-order cores that give rise to the formation of $\pm 1/2$ disclination pairs [Fig. 13(b)] as ridges form between adjacent roll cells. As the director wags between the compression and extension quadrants of the shear plane, ridge-splitting occurs at the ends of the ridge to create a ± 1 pairs of disclinations [Fig. 13(c)]. As is indi-

cated by the fact that the subsequent ± 1 pair of disclinations in Fig. 13(d) have low-order cores, ridge-splitting leads to low-order defect pairs when the director lies within the compression quadrant during the splitting process and the escaped configuration when the director is oriented within the extension quadrant. As ± 1 pairs of disclinations are continually generated between adjacent roll cells, defects annihilate via recombination in the compression regions [e.g., the ± 1 defect pair at $y \approx 0.6$ in Fig. 13(d)], but remain somewhat stationary in the extension regions. This process continues, forming up to as many as four ± 1 disclination pairs propagating inward from the upper and lower domain boundaries, until the irregularity of the flow structure and polymer dynamics is such that there is little discernible structure within the domain.

4. Disclination predictions versus experiment and the predictions of the LE theory

In considering the mechanisms by which disclinations form and the local orientation structure in the vicinity of disclination cores, we are limited by the fact that there are no available experimental data that provide details of the microstructure at such small scales. Hence, we can only provide qualitative comparisons between predictions of the DMG model and experimental observations. Comparisons with previous theoretical predictions are also limited, since the most comprehensive of these are based on the LE model,

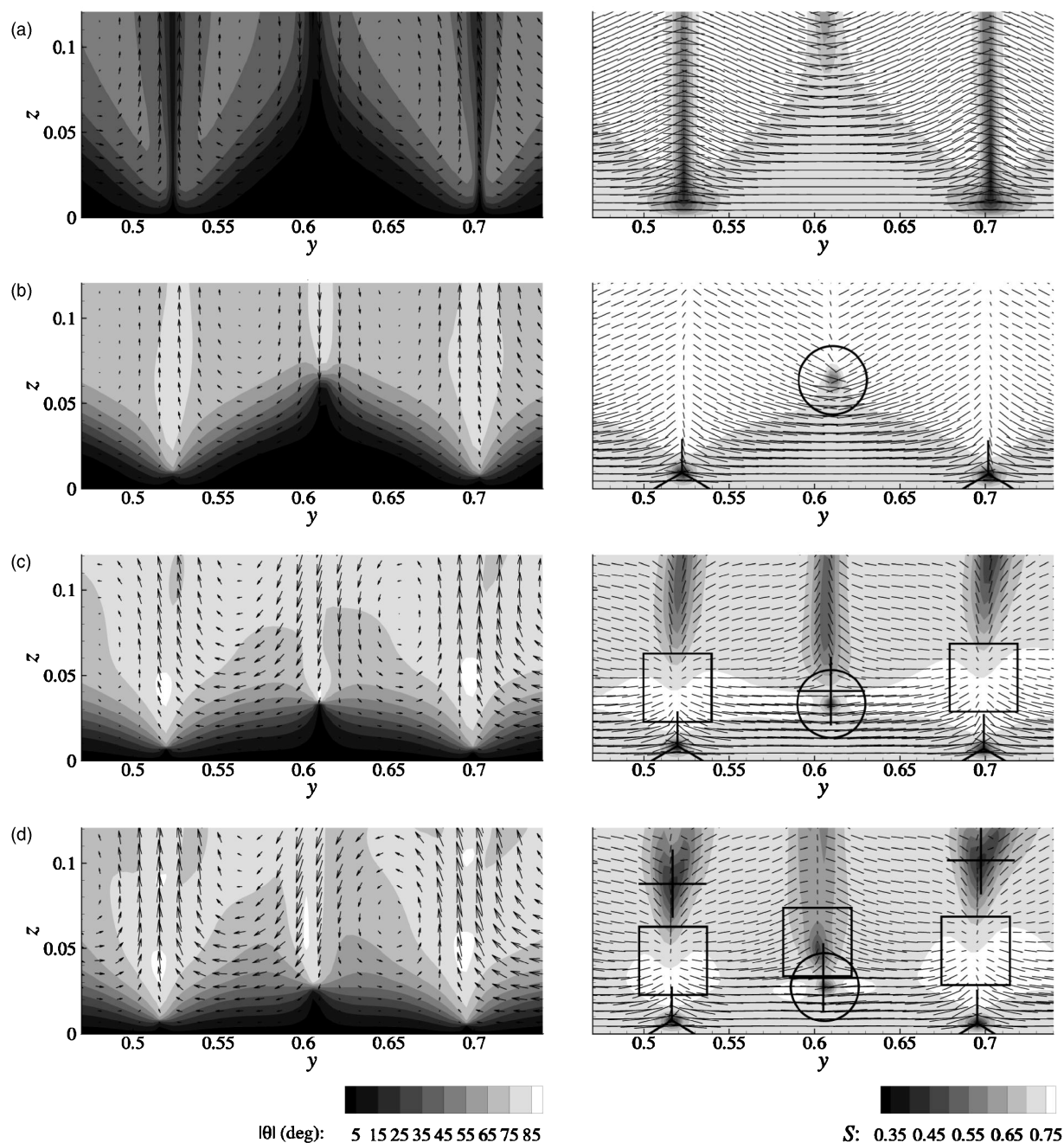


FIG. 13. Early-stage disclination formation for $Er=5000$ ($De=5$). (left) Secondary flow vector field (v_y, v_z) and tip angle magnitude $|\theta|$ scalar contour and (right) director vector field $\mathbf{d}(\mathbf{x})$ and order parameter S scalar contour at (a) $\tau=9$, (b) $\tau=16$, (c) $\tau=27$, and (d) $\tau=31$ strain units. The three-armed symbols and circles indicate the $-1/2$ and $+1/2$ disclinations, respectively. The crosses and squares indicate the -1 and $+1$ disclinations, respectively. Note: a color animation of the process depicted in this sequence of images is available online.

which neglects viscoelasticity, and is thus intrinsically restricted from predicting the formation of $1/2$ -strength defects. Comparison of our results to those of Feng *et al.*,²⁷ in the context of the mechanisms of disclination formation, is limited to that of ± 1 disclinations. Given that the DMG model reduces to the LE model as $De \rightarrow 0$, it is not surprising that the ± 1 disclination pairs observed at relatively low Er form by the same ridge-splitting mechanism that was first identified by Feng *et al.* Given the complexity that the solution exhibits for moderate to high Er , it is, however, somewhat surprising that this mechanism was universal through-

out our calculations. With regard to the life span of $\pm 1/2$ defects, there is also quantitative agreement between the predictions of the DMG and LE models.

Although the $\pm 1/2$ disclination mechanism cannot be validated against available experimental or numerical data, a promising feature of the $1/2$ -strength defects observed in our calculations is their location. Larson and Mead¹¹ reported that defects usually originate and reside between adjacent roll cells. In accordance with Larson and Mead's observations, whether between daughter cells formed during the roll-cell splitting process ($Er \lesssim 1500$) or along the domain bound-

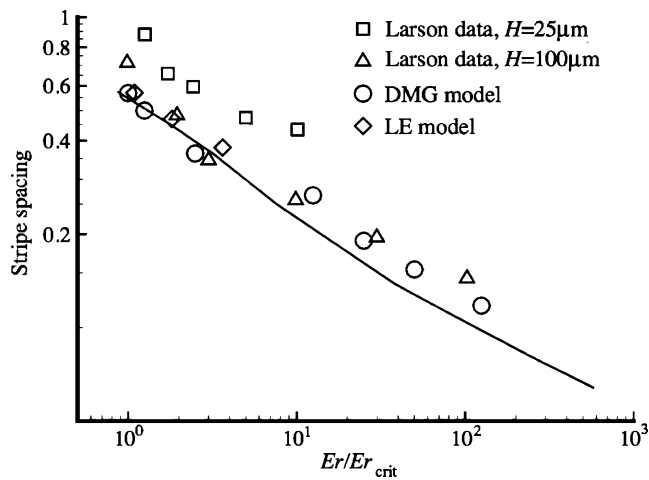


FIG. 14. Spacing of (strain-averaged) birefringent stripes, scaled by the gap width, versus scaled Er for the experimental observations of Larson and Mead,¹¹ our DMG model results, and LE theory results reported by Feng *et al.*²⁷ The line represents the predictions of the linear stability analysis of the LE theory.²⁶

aries between adjacent roll cells ($1500 \leq Er \leq 6000$), $\pm 1/2$ disclinations were generally found to originate and reside between roll cells. For $Er \leq 1500$, there is an apparent discrepancy between the predictions of the DMG theory and the experimental observations of Larson and Mead for the case of ± 1 disclination pairs, in the sense that these form at the core of the roll cells instead of between them. However, for $1500 \leq Er \leq 6000$, 1-strength defects were found to originate between adjacent roll cells.

5. Evaluation of steady-state band spacing predictions for low to moderate Er

Given the uncertainty of the material parameters for the PBG solutions used in the experimental systems and differences between those used in our calculations and those used in the LE calculations, quantitative comparisons between the steady-state band spacing predictions of the DMG model and the experimental data reported by Larson and Mead¹¹ and the numerical results of Larson²⁶ and Feng *et al.*²⁷ will be based on the ratio Er/Er_{crit} , where Er_{crit} is the Ericksen value for which the perturbed system becomes unstable to the formation of roll cells. For quantitative comparison of the predicted steady-state band spacing, we calculate the birefringence pattern in the same manner as was employed by Sgalari *et al.*¹⁴ In Fig. 14, we present the steady-state spacing of birefringence stripes, scaled by the gap width, as a function of the scaled Ericksen number Er/Er_{crit} for the experimental observations of Larson and Mead, our DMG model results, LE model results reported by Feng *et al.*, and the prediction of Larson's LE theory stability analysis. For $Er/Er_{crit} \geq 6$, where an irregular flow and orientation structure persists, band-spacing values are those associated with the dominant wave number of the birefringence pattern, as determined from the strain-averaged power spectrum generated using FFTs after the solution reached a quasistationary state. As is evident from the data presented in Fig. 14, there is good quantitative agreement between the steady-state band

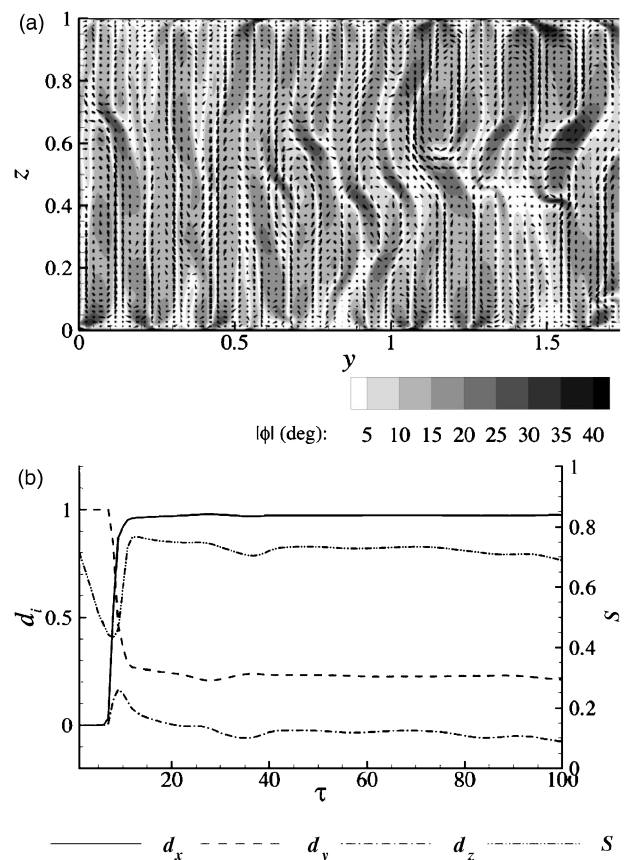


FIG. 15. (a) Secondary flow vector field (v_y, v_z) and tip angle magnitude $|\phi|$ scalar contour at $\tau=35$ strain units and (b) director components d_i and order parameter S as a function of strain units τ at $(y, z) = (0.26, 0.25)$ for $Er = 10000$ ($De = 10$). Note: a color animation showing the evolution of the flow and tip angle is available online.

spacing predicted by the DMG model and the experimental values over a large range of Ericksen values.

B. High shear rates, $Er \geq 10000$ ($De \geq 10$)

As we continue to increase Er (and De), the initial roll-cell structure becomes increasingly transitory, and the irregular flow patterns and microstructure that develop give rise to a preponderance of the $1/2$ - and 1-strength disclinations and eddies of decreasing sizes and strengths, characteristic of director turbulence.^{44–47} This refinement continues until, at $Er \approx 10000$ ($De \approx 10$), the solution exhibits neither disclinations nor roll cells. The system does, however, retain some structure along the spanwise direction that has the visual appearance of stripes. Specifically, there is a modulation in the mean orientation away from the shear plane along the y axis; the angle between the director and shear plane is given as ϕ (not to be confused with θ , the angle between \mathbf{d} and the y - z plane). As an example of the striped texture observed at high shear rates, we present a snapshot of the secondary flow and banded structure associated with the modulation in the director field for $Er = 10000$ ($De = 10$) at $\tau = 35$ strain units in Fig. 15(a), where the maximum secondary velocity magnitude is 0.009 and, away from the upper and lower domain boundaries, $0 \leq |\phi| \leq 35$ degrees. This solution is representative of the quasistationary state (quasistationary in the sense that the

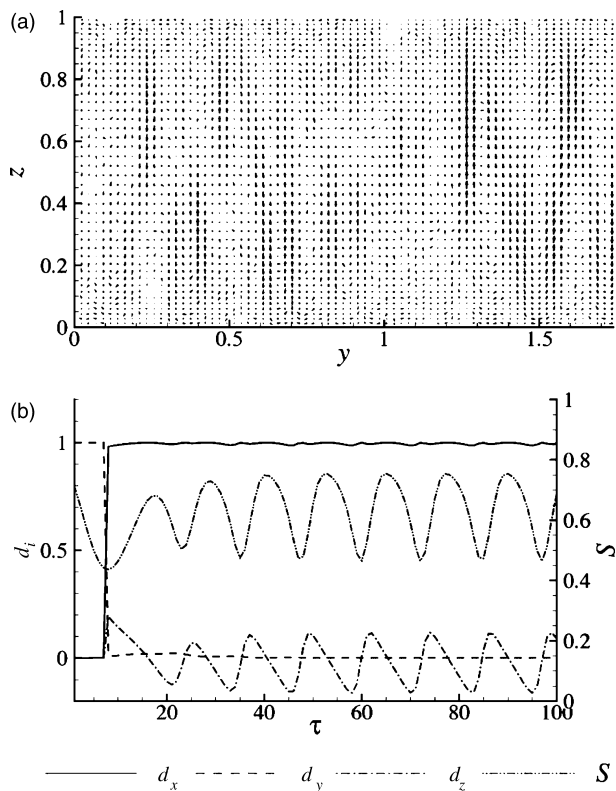


FIG. 16. (a) Secondary flow vector field (v_y, v_z) at $\tau=35$ strain units and (b) director components d_i and order parameter S as a function of strain units τ at $(y, z)=(1.00, 0.50)$ for $Er=12500$ ($De=12.5$).

general structure persists for the entire duration of our simulation, up to $\tau=100$ strain units) reached at approximately $\tau=25$ strain units. Although in regions in which the director orientation is almost parallel to the shear plane, as indicated by the white vertical bands in the $|\phi|$ contour in Fig. 15(a), the director exhibits wagging, the director orientation remains relatively stationary in regions highlighted by dark vertical bands, where $|\theta| \geq 5$ degrees, after the solution reaches (quasi)steady state [cf. Fig. 15(b)].

The dynamics and structure described above are precisely those reported by Larson and Mead¹¹ that correspond to the transition between the Ericksen and Deborah number cascades, wherein the system is stabilized by viscoelasticity and the texture refinement associated with gradient elasticity subsides and there is the reappearance of a striped texture similar to that observed at low shear rates within the Ericksen number cascade. As verified by Larson and Mead using polarizing microscopy, the banded pattern resulted from modulations in the mean orientation away from the shear plane along the y axis. We should note that, although the orientation structure was not investigated, similar high-shear-rate banded structures have also been reported by Guido, Frallicciardi, Grizzuti, and Marrucci,⁴⁸ for aqueous solutions of HPC (hydroxypropylcellulose), and Tan and Berry,¹³ for solutions of PPTA [poly(1,4-phenylene terephthalamide)].

As we further increase Er (and De), although the spanwise length scale of the banded structure does not exhibit a dependence on Er , the amplitude of the modulation in ϕ decreases until, at $Er \approx 12000$ ($De \approx 12$), the director at each

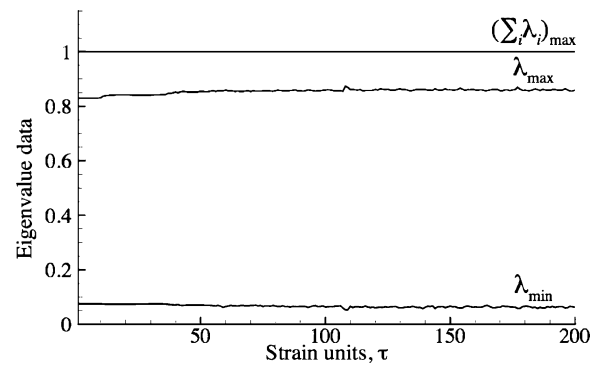


FIG. 17. Eigenvalue data versus strain units for $Er=2000$ simulation.

material point in the domain lies within the shear plane. Henceforth, we refer to this transition as the “shear-aligning” transition. In Fig. 16, we show an example of the secondary flow for $Er=12500$ ($De=12.5$) at $\tau=35$ strain units, where the maximum secondary velocity magnitude is 0.002, and the evolution of the director components and order parameter at $(y, z)=(1.00, 0.50)$, an arbitrarily chosen point within the domain. We should note that the unapproximated Doi theory³⁰ exhibits flow-aligning, where the director assumes a steady-state orientation along the flow axis, for De of this magnitude. As is highlighted by the dynamics of the director and order parameter in Fig. 16(b), the Bingham closure approximation simply predicts wagging, where the director oscillates about a fixed angle, with an amplitude that decreases monotonically with increasing De . This deficiency in the closure approximation used in our calculations does not, however, limit the model’s ability to capture the shear-aligning transition observed experimentally by Larson and Mead.¹¹

IV. CONCLUSION

As a summary of the findings of our investigation, for planar shear flow, the DMG model was found to exhibit dynamics in both qualitative and quantitative agreement with experimental observations reported in the literature for the so-called Ericksen number and Deborah number cascades. Within the Ericksen number cascade, where the dominant contribution to the stress is that of gradient elasticity, for

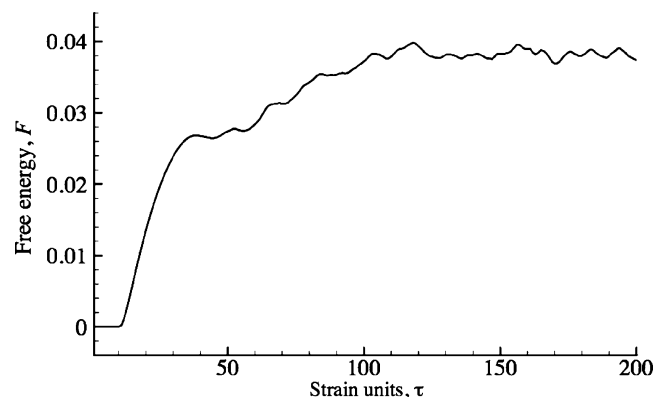


FIG. 18. Free-energy eigenvalue data versus strain units for $Er=2000$ simulation. The free energy F has been scaled by $\nu k_B TA$, where A is the dimensionless area of the computational domain.

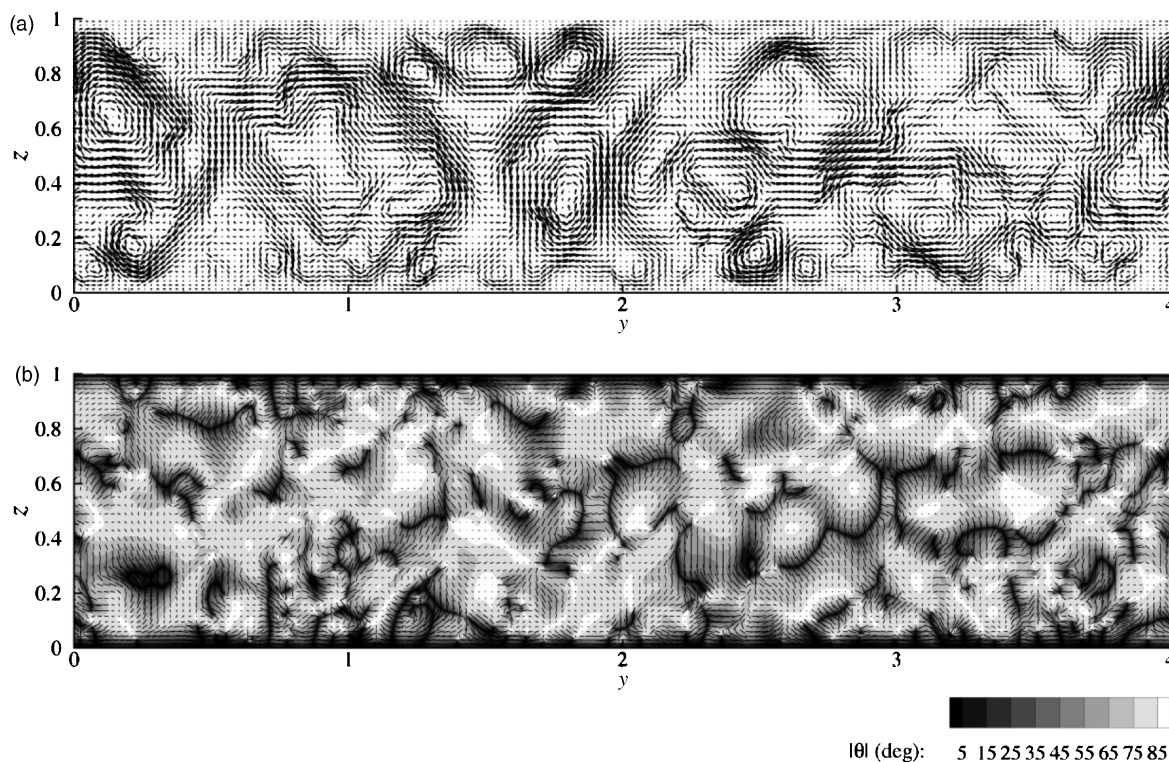


FIG. 19. (a) Secondary flow vector field (v_x, v_y) and (b) director vector field $\mathbf{d}(\mathbf{x})$ and tip angle magnitude $|\theta|$ at $\tau=200$ strain units for $Er=2000$.

increasing shear rates, the DMG model displayed three regimes: stable simple shear, stable roll cells, and irregular structure accompanied by disclination formation. For increasing shear rates within the Deborah number cascade, where viscoelasticity is the dominant stress contribution, the DMG model exhibits two regimes: a streamwise banded structure, in the absence of roll cells and disclinations, and shear alignment, where the mean orientation lies within the shear plane throughout the domain.

The DMG model was found to predict both 1- and $1/2$ -strength disclinations. The formation of $\pm 1/2$ defects is a response of the system to an imposed curvature along either a localized region, as was observed in our low Er calculations, or delocalized regions such as the low-order regions between adjacent roll cells observed at moderate Er values. Similarly, ± 1 disclination pairs either formed from localized ridges, resulting in an escaped configuration, or emanated from the ends of large-scale ridges via the same *ridge-splitting* mechanism identified by Feng *et al.*²⁷ using the Leslie-Ericksen model. Given that the DMG model reduces to the LE model as $De \rightarrow 0$, it is not surprising that the ± 1 disclination pairs observed at relatively low Er form by the same ridge-splitting mechanism that was first identified by Feng *et al.* Disclinations of strength $\pm 1/2$, however, have not previously been predicted in flow simulations, and thus may be seen as a major accomplishment for both the DMG model of LCPs and the computational procedures developed in this work. It is somewhat surprising that the mechanisms by which ± 1 and $\pm 1/2$ disclination pairs formed was universal throughout the entire region of the Er - De parameter space explored in our investigation, particularly

given the complexity that the solution exhibits for moderate to high Er .

In conclusion, we have verified that the DMG molecular theory for LCPs is capable of predicting the onset and evolution of both types of disclinations seen experimentally, and is capable of qualitatively reproducing the Ericksen and Deborah number cascades in a simple, two-dimensional shear cell. Additionally, the results have validated the computational tools developed in this study. We are therefore prepared to extend this investigation to fully three-dimensional calculations so as to fully explore the predictive capabilities of the DMG theory.

ACKNOWLEDGMENTS

The primary sources of funding for this work were the National Science Foundation (NSF), through IGERT Grant No. DGE02-21715, and a grant to L.G.L. from the Unilever Corporation. The participation of H.D.C. and C.J.G.-C. in this project was supported, respectively, via Grant No. DMS-0311911 and Grants No. DMS-0411504 and No. DMS-0505738 from the NSF. The computations presented in this paper were carried out at UCSB on a Beowulf cluster purchased with funding from the aforementioned NSF IGERT grant in the Computer Science Department and a Beowulf cluster in the Mathematics Department purchased with funding from NSF SCREMS Grant No. DMS-0112388.

APPENDIX: NUMERICAL CHALLENGES

As is the case for viscoelastic flow calculations in general, two issues must be addressed when choosing an inte-

gration scheme: stability and preservation of the positive definiteness of the configuration tensor \mathbf{A} . In addition to concerns associated with numerical stability, which are defined in terms of the standard CFL constraints on the allowable time step, in simulating the dynamics of polymeric fluids, the discretized form of the governing equations can become ill-posed if the accuracy of the method cannot ensure that the positive definiteness of \mathbf{A} is maintained. Therefore, in surveying the literature, one finds this to be the leading topic addressed in simulating non-Newtonian flows. Given the complex (nonlinear) form of the governing equation for the dynamics of \mathbf{A} (7), we have restricted ourselves to the use of an explicit integration scheme. In considering integration schemes, we found that the explicit Euler or standard second- and third-order Runge-Kutta methods⁴⁹ required the use of unreasonably small time steps [$\mathcal{O}(10^{-6})$ or smaller]. This constraint was alleviated by using the second-order Runge-Kutta TVD scheme proposed by Shu and Oscher,⁴² which inherently limits the growth of grid-level oscillations. For the results presented in this work, $10^{-4} \leq \Delta t \leq 10^{-3}$. To highlight the fact that we maintain the positive-definiteness of \mathbf{A} , we show the strain evolution of the minimum and maximum eigenvalues of \mathbf{A} , λ_{\min} and λ_{\max} , respectively, and $|\sum_{i=1}^3 \lambda_i|_{\max}$ for our $Er=2000$ calculation in Fig. 17. With regard to the eigenvalues, it is clear that they are all positive, and the sum $\sum_{i=1}^3 \lambda_i = 1$. The second-order tensor \mathbf{A} , which is symmetric, therefore remains positive-definite throughout the simulation.

The stability of the solution can also be monitored by considering the evolution of the system's free energy F , which, in the context of the DMG theory, can be written as

$$F = \int_A \nu \left[k_B T \langle \ln \psi(\mathbf{u}; \mathbf{r}) \rangle + \frac{1}{2} \langle \phi_{MG}(\mathbf{u}; \mathbf{r}) \rangle \right] dA, \quad (\text{A1})$$

where the domain area A is scaled by H^2 . For the Bingham closure approximation, $\psi(\mathbf{u}; \mathbf{r})$ takes the form³⁶

$$\psi_b(\mathbf{u}; \mathbf{r}) = \frac{1}{Z} \exp(\mathbf{u} \cdot \mathbf{T} \cdot \mathbf{u}), \quad (\text{A2})$$

where $Z = \int_{S^2} \exp(\mathbf{u} \cdot \mathbf{T} \cdot \mathbf{u}) d\mathbf{u}$ and the symmetric tensor \mathbf{T} is defined such that its eigenvectors and those of the second moment \mathbf{A} are coaligned. The free energy, evaluated using the Bingham closure approximation and the nematic potential proposed by Marrucci and Greco (3), is therefore

$$F = \nu k_B T \int_A \left[\mathbf{T} : \mathbf{A} - \ln Z - \frac{3}{4} U \left(\mathbf{A} + \frac{\ell^2}{24} \nabla^2 \mathbf{A} \right) : \mathbf{A} \right] dA - F_0, \quad (\text{A3})$$

where F_0 is the equilibrium value of the free energy in the absence of flow and spatial gradients. Since the entropic contribution, $\mathbf{T} : \mathbf{A} - \ln Z$, cannot be expressed analytically in terms of \mathbf{A} , it is calculated using a fitting function generated in a manner similar to that used to calculate the components of the fourth moment \mathbf{Q} for the Bingham closure approximation. In Fig. 18, we show the evolution of the nondimensional free energy, where the free energy F is scaled by $\nu k_B T A$, for our $Er=2000$ calculation. As a result of the im-

posed shear, the free energy increases monotonically until $\tau \approx 37$ strain units, when the formation of the first $\pm 1/2$ pair of disclinations alleviates stresses imposed by distortions in the director field. With increasing strain, the free energy continues to increase, exhibiting modulations as defects form and annihilate and the director field is continually perturbed, until a quasistationary state is reached at $\tau \approx 105$ strain units. Ultimately, it is bounded, further highlighting the fact that the solution remains accurate for the duration of the simulation. In conclusion, as an example of the complexity of the flow and microstructure that develops in our calculations, we show a snapshot of the secondary flow and director field for $Er=2000$ at $\tau=200$ strain units in Fig. 19.

¹S. Chandrasekhar, *Liquid Crystals*, 2nd ed. (Cambridge University Press, Cambridge, UK, 1992).

²P. G. de Gennes and J. Prost, *The Physics of Liquid Crystals*, 2nd ed. (Oxford University Press, London, 1993).

³A. M. Donald and A. H. Windle, *Liquid Crystalline Polymers* (Cambridge University Press, Cambridge, UK, 1992).

⁴F. C. Frank, "On the theories of liquid crystals," *Discuss. Faraday Soc.* **25**, 19 (1958).

⁵M. Reiner, "The Deborah number," *Phys. Today* **17** (1), 62 (1964).

⁶G. Kiss and R. S. Porter, "Rheo-optical studies of liquid-crystalline solutions of helix polypeptides," *Mol. Cryst. Liq. Cryst.* **60**, 267 (1980).

⁷B. Ernst and P. Navard, "Band textures in mesomorphic (hydroxypropyl) cellulose solutions," *Macromolecules* **22**, 1419 (1989).

⁸M. Srinivasarao and G. C. Berry, "Rheo-optical studies on aligned nematic solutions of a rodlike polymer," *J. Rheol.* **35**, 379 (1991).

⁹J. T. Gleeson, R. G. Larson, D. W. Mead, G. Kiss, and P. E. Cladis, "Image analysis of shear-induced textures in liquid-crystalline polymers," *Liq. Cryst.* **11**, 341 (1992).

¹⁰R. G. Larson and D. W. Mead, "Development of orientation and texture during shearing of liquid-crystalline polymers," *Liq. Cryst.* **12**, 751 (1992).

¹¹R. G. Larson and D. W. Mead, "The Ericksen number and Deborah number cascades in sheared polymeric nematics," *Liq. Cryst.* **15**, 151 (1993).

¹²J. Vermant, P. Moldenaers, S. J. Picken, and J. Mewis, "A comparison between texture and rheological behaviour of lyotropic liquid crystalline polymers during flow," *J. Non-Newtonian Fluid Mech.* **53**, 1 (1994).

¹³Z. Tan and G. C. Berry, "Studies on the texture of nematic solutions of rodlike polymers. 3. Rheo-optical and rheological behavior in shear," *J. Rheol.* **47**, 73 (2002).

¹⁴G. Sgalari, L. G. Leal, and E. Meiburg, "Texture evolution of sheared liquid crystalline polymers: Numerical predictions of roll-cells instability, director turbulence, and striped texture with a molecular model," *J. Rheol.* **47**, 1417 (2003).

¹⁵G. Marrucci and F. Greco, "The elastic constants of Maier-Saupe rodlike molecule nematics," *Mol. Cryst. Liq. Cryst.* **206**, 17 (1991).

¹⁶J. Feng, G. Sgalari, and L. G. Leal, "A theory for flowing nematic polymers with orientational distortion," *J. Rheol.* **44**, 1085 (2000).

¹⁷R. Zhou, M. G. Forest, and Q. Wang, "Kinetic structure simulations of nematic polymers in plane Couette cells. I: The algorithm and benchmarks," *Multiscale Model. Simul.* **3**, 853 (2005).

¹⁸G. Sgalari, L. G. Leal, and J. J. Feng, "The shear flow behaviour of LCPs based on a generalized Doi model with distortional elasticity," *J. Non-Newtonian Fluid Mech.* **102**, 361 (2002).

¹⁹R. Kupferman, M. N. Kawaguchi, and M. M. Denn, "Emergence of structure in a model of liquid crystalline polymers with elastic coupling," *J. Non-Newtonian Fluid Mech.* **91**, 255 (2000).

²⁰T. Tsuji and A. D. Rey, "Effect of long range order on sheared liquid crystalline materials: Flow regime transitions and rheological phase diagrams," *Phys. Rev. E* **62**, 8141 (2000).

²¹T. Tsuji and A. D. Rey, "Orientational mode selection mechanisms for sheared nematic liquid crystalline materials," *Phys. Rev. E* **57**, 5609 (1998).

²²A. D. Rey and T. Tsuji, "Recent advances in theoretical liquid crystal rheology," *Macromol. Theory Simul.* **7**, 623 (1998).

²³T. Tsuji and A. D. Rey, "Effect of long range order on sheared liquid crystalline materials. Part 1: Compatibility between tumbling and behaviour and fixed anchoring," *J. Non-Newtonian Fluid Mech.* **73**, 127 (1997).

- ²⁴P. T. Mather, D. S. Pearson, and R. G. Larson, "Flow patterns and disclination-density measurements in sheared nematic liquid crystals II: Tumbling 8CB," *Liq. Cryst.* **20**, 539 (1996).
- ²⁵Calculations performed by W. H. Han and A. D. Rey [Macromolecules **28**, 8401 (1995)] using the phenomenologically based Leslie-Ericksen theory, in which gradients along the spanwise direction are neglected and the domain lies within the shear plane, predict a flow and orientation structure that corresponds to a spanwise-oriented banded texture.
- ²⁶R. G. Larson, "Roll-cell instabilities in shearing flows of nematic polymers," *J. Rheol.* **37**, 175 (1993).
- ²⁷J. J. Feng, J. Tao, and L. G. Leal, "Roll cells and disclinations in sheared nematic polymers," *J. Fluid Mech.* **449**, 179 (2001).
- ²⁸J. L. Ericksen, "Conservation laws for liquid crystals," *Trans. Soc. Rheol.* **5**, 23 (1961).
- ²⁹F. M. Leslie, "Some constitutive equations for liquid crystals," *Arch. Ration. Mech. Anal.* **28**, 265 (1968).
- ³⁰M. Doi, "Molecular dynamics and rheological properties of concentrated solutions of rodlike polymers in isotropic and liquid crystalline phases," *J. Polym. Sci., Polym. Phys. Ed.* **19**, 229 (1981).
- ³¹M. Doi and S. F. Edwards, *The Theory of Polymer Dynamics* (Oxford University Press, New York, 1986).
- ³²R. B. Bird, C. F. Curtis, R. C. Armstrong, and O. Hassager, *Dynamics of Polymeric Fluids, Vol. 2: Kinetic Theory*, 2nd ed. (John Wiley and Sons, New York, 1987).
- ³³W. Maier and A. Saupe, "Eine einfache molekular-statistische theorie der nematischen kristallinflüssigen phase. I," *Z. Naturforsch. A*, **14**, 882 (1958).
- ³⁴W. Maier and A. Saupe, "Eine einfache molekular-statistische theorie der nematischen kristallinflüssigen phase. I," *Z. Naturforsch. A*, **15**, 288 (1960).
- ³⁵S. Prager, "Stress-strain relationship in a suspension of dumbbells," *Trans. Soc. Rheol.* **1**, 53 (1957).
- ³⁶C. V. Chaubal and L. G. Leal, "A closure approximation for liquid-crystalline polymer models based on parametric density estimation," *J. Rheol.* **42**, 177 (1998).
- ³⁷J. Feng, C. V. Chaubal, and L. G. Leal, "Closure approximations for the Doi theory: Which to use in simulating complex flows of liquid-crystalline polymers," *J. Rheol.* **42**, 1095 (1998).
- ³⁸J. Feng and L. G. Leal, "Pressure-driven channel flows of a model liquid-crystalline polymer," *Phys. Fluids* **11**, 2821 (1999).
- ³⁹M. Vinokur, "On one-dimensional stretching functions for finite-difference calculations," *J. Comput. Phys.* **50**, 215 (1983).
- ⁴⁰H. A. van der Vorst, "Bi-CGSTAB: A fast and smoothly converging variant of Bi-CG for the solution of nonsymmetric linear systems," *SIAM (Soc. Ind. Appl. Math.) J. Sci. Stat. Comput.* **13**, 631 (1992).
- ⁴¹D. H. Klein, C. J. Garcia-Cervera, H. D. Cenicerros, and L. G. Leal, "Computational studies of the shear flow behavior of a model for liquid crystalline polymers," *Proceedings of the 12th Computational Techniques and Applications Conference CTAC-2004* (ANZIAM, 2005), Vol. 46, pp. C210-C244.
- ⁴²C. Shu and S. Osher, "Efficient implementation of essentially non-oscillatory shock-capturing schemes," *J. Comput. Phys.* **77**, 439 (1988).
- ⁴³P. Manneville and E. Dubois-Violette, "Shear flow instability in nematic liquids: Theory steady simple shear flows," *J. Physique* **37**, 285 (1976).
- ⁴⁴P. Pieranski and E. Guyon, "Instability of certain shear flows in nematic liquids," *Phys. Rev. A* **9**, 404 (1974).
- ⁴⁵P. Manneville, "The transition to turbulence in nematic liquid crystals," *Mol. Cryst. Liq. Cryst.* **70**, 1501 (1981).
- ⁴⁶P. E. Claudis and S. Torza, "Flow instabilities in Couette flow in nematic liquid crystals," in *Colloid and Interface Science*, edited by M. Kelker (Academic, New York, 1976), Vol. 4, p. 487.
- ⁴⁷P. E. Cladis and W. van Saarloos, "Some nonlinear problems in anisotropic liquids," in *Solitons in Liquid Crystals*, edited by L. Lam and J. Prost (Springer-Verlag, New York, 1990).
- ⁴⁸S. Guido, P. Frallicciardi, N. Grizzuti, and G. Marrucci, "Rheo-optics of hydroxypropylcellulose solutions in Poiseuille flow," *Rheol. Acta* **33**, 22 (1994).
- ⁴⁹*Computational Techniques for Fluid Dynamics: Fundamental and General Techniques*, edited by C. A. J. Fletcher, R. Glowinski, and M. Holt (Springer-Verlag, New York, 1991), Vol. 1.